Dynamic Instability of Dendrite Tips Generates the Highly Branched Morphologies of Sensory Neurons

Sonal Shree[1]*, Sabyasachi Sutradhar[1]*, Olivier Trottier[1,2], Yuhai Tu[3], Xin Liang[4], and Jonathon Howard[1,2,5,#]

[1]Department of Molecular Biophysics & Biochemistry, Yale University, New Haven, CT 06511
[2]Department of Physics, Yale University, New Haven, CT 06511
[3]IBM T.J. Watson Research Center, Yorktown Heights, NY 10598
[4]Tsinghua-Peking Joint Center for Life Sciences, School of Life Sciences, Tsinghua University, 100084 Beijing, China
[5]Quantitative Biology Institute, Yale University, New Haven, CT 06511

*These authors contributed equally [#]Correspondence: joe.howard@yale.edu

Summary

The highly ramified arbors of neuronal dendrites provide the substrate for the high connectivity and computational power of the brain. Altered dendritic morphology is associated with neuronal diseases. Many molecules have been shown to play crucial roles in shaping and maintaining dendrite morphology. Yet, the underlying principles by which molecular interactions generate branched morphologies are not understood. To elucidate these principles, we visualized the growth of dendrites throughout larval development of *Drosophila* sensory neurons and discovered that the tips of dendrites undergo dynamic instability, transitioning rapidly and stochastically between growing, shrinking, and paused states. By incorporating these measured dynamics into a novel, agent-based computational model, we showed that the complex and highly variable dendritic morphologies of these cells are a consequence of the stochastic dynamics of their dendrite tips. These principles may generalize to branching of other neuronal cell-types, as well as to branching at the subcellular and tissue levels.

Key words

Branching morphogenesis, neuronal development, dendrite, arbor, dynamic instability, agent-based model

Introduction

Neurons are polarized cells (Cajal, 1906) whose axons and dendrites are often highly branched. Branching provides the surface area necessary for dendrites to receive inputs from thousands of other cells or from the environment (Lefebvre et al., 2013), and for axons to output signals to multiple cells. In this way, branching facilitates the high connectivity of the brain (Lefebvre et al., 2013). The morphology of the neurons, together with their synaptic connections (Fornito et al., 2015; Kandel et al., 2013; Seung, 2012; Zheng et al., 2018), defines the structure of the nervous system, the

connectome, which is viewed as a prerequisite for understanding brain function (Denk et al., 2012). Knowing the rules of neuronal branching is expected to facilitate mapping the connectome by providing anatomical constraints or laws, as well as giving insight into genetic disorders that affect morphology (Forrest et al., 2018; Kapitein and Hoogenraad, 2015; Koleske, 2013; Kulkarni and Firestein, 2012; Moughamian and Holzbaur, 2017). Whereas much is known about the growth of axons, whose tips, the growth cones, are guided by extracellular signals and guidepost cells (Lowery and Vactor, 2009; Sánchez-Soriano et al., 2007; Stoeckli, 2018; Tessier-Lavigne and Goodman, 1996), the mechanisms underlying the growth and branching of dendrites is poorly understood.

While many molecules have been shown to play crucial roles in shaping and maintaining dendrite morphology, the underlying principles by which molecular interactions generate branched morphologies is not understood. To elucidate these rules, we have focused on dendrite morphogenesis in class IV dendritic arborization (da) neurons in *Drosophila*, a model system for dendritogenesis (Dong et al., 2015; Jan and Jan, 2010; Singhania and Grueber, 2014). These nociceptive neurons form a highly branched meshwork just under the cuticle that senses puncture of the larva by the ovipositor barbs of parasitic wasps and initiates avoidance behaviors (Basak et al., 2021; Robertson et al., 2013). Class IV cells are ideal for studying branching morphogenesis because they grow rapidly over 5 days of larval development, their branches are non-crossing due to self-avoidance mediated by the Down's syndrome cell adhesion molecule (Hughes et al., 2007; Matthews et al., 2007; Soba et al., 2007) and other molecules (Emoto et al., 2004; Parrish et al., 2009), and can be visualized using cell-specific labeling (Grueber et al., 2003; Jan and Jan, 2010). Many molecules that participate in dendrite morphogenesis have been identified: transcription factors (Jinushi-Nakao et al., 2007); extracellular matrix and integrins (Han et al., 2012; Kim et al., 2012); actin-associated proteins (Lee et al., 2003; Li and Gao, 2003; Scott et al., 2003; Stürner et al., 2019); microtubule motors such as dynein and kinesin (Arthur et al., 2015; Satoh et al., 2008; Zheng et al., 2008); microtubule regulators such as spastin (Sherwood et al., 2004), katanin (Stewart et al., 2012) and γ-tubulin (Ori-McKenney et al., 2012); and microRNAs such as *bantam* (Parrish et al., 2009). The major difficulty,

however, is that it is currently not possible to make a mechanistic connection between developmental processes occurring at the molecular and subcellular levels, and the morphology of the entire dendritic arbor.

While several theoretical and computational models can predict dendrite-like branched morphologies, they are not grounded in molecular or development processes data. Early models, designed to describe and classify neurons, reconstituted morphologies based on the statistical properties of the observed arbors themselves (Ascoli and Krichmar, 2000; Nanda et al., 2018). Optimization-based models that minimize wiring (i.e., the total lengths of the branches) capture key features of neuronal morphology (Baltruschat et al., 2020; Cuntz et al., 2010), but lack connection to the molecular processes. Other models use hypothetical branching properties (Ganguly et al., 2016; Palavalli et al., 2021), or abstract processes such as diffusion-limited aggregation (Luczak, 2006), or Turing-like pattern formation (Sugimura et al., 2007). On the other hand, branching models developed for tissues such as the lungs (Metzger et al., 2008) and kidneys (Lefevre et al., 2017; Short et al., 2014), produce stereotyped morphologies that differ from the highly variable morphologies of neurons (Kanari et al., 2018). Stochastic models developed for other tissues, such as the mammary glands, use properties that are specific to these systems, such as tip bifurcation (Hannezo et al., 2017). Thus, current computational models fall short in providing a mechanistic understanding of dendrite morphology.

To circumvent these limitations, we have formulated a computational model that is based entirely on experimentally observed properties of dendrites measured over their development. The data-based model takes as input tip-growth dynamics, branching rates and self-avoidance measured using high-resolution, live-cell imaging in the developing animal. The model successfully recapitulates class IV dendrite morphogenesis and shows how the complex and variable morphology of dendritic arbors emerge from the microscopic dynamics of dendrite tips and provides insights into several mutant phenotypes.

Results

As *Drosophila* larvae grow (Figure 1A), the arbors of their class IV dendrites also grow (Figure 1B). By the end of larval development, the meshwork of branches covers the larval surface like chainmail and the individual dendritic arbors fill the eight abdominal segments with cell widths up to 500 µm. When the first instar larva hatches at 24 hr after egg-lay (egg-lay is defined as time zero), the dendritic arbors are smaller than the segments in which they are located. Over the next 24 hr, the arbors grow faster than the segments and touch the segment boundaries in a process called tiling (Grueber et al., 2002); at 72 hr the arbor densely fills the segment (Parrish et al., 2009) and then grows at the same rate as the segments (Figure 1, inset). We sought to understand how dendrites tile and infill.

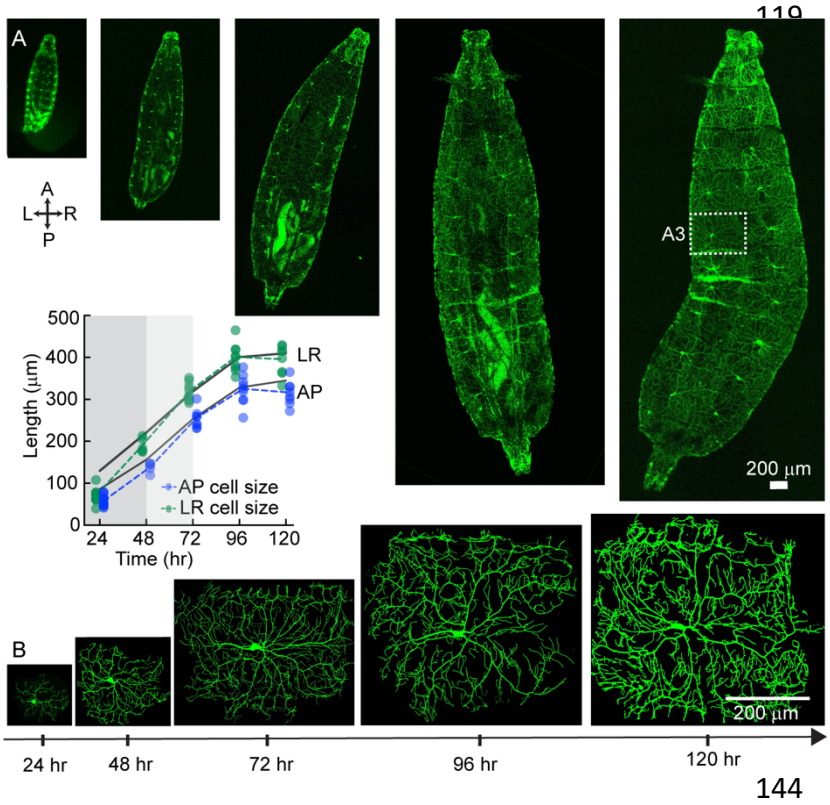

Figure 1. Growth of larvae and class IV neurons over development. A Whole-mount, living larvae imaged by spinning-disk confocal microscopy at 24 hr to 120 hr (egg-lay defined as time zero). Anterior (A) is up and posterior (P) down. Left (L) and right (R) as viewed from the dorsal side (Methods). Class IV neurons are marked with the transmembrane protein CD4 tagged with GFP (;;ppkCD4-tdGFP). **B** Individual class IV cells from the A3 or A4 segments. An A3 segment is outlined in A (120 hr). **Inset** At 24 hr, the cell widths (filled circles and dashed lines) are smaller than the segment (filled lines). In the next 24 hr, they touch the growing segment boundaries (dark gray) and infill by 72 (light gray).

Uniform branch dilation cannot account for dendrite arbor growth

We first asked whether class IV arbors grow through dilation of their branches (Figure 2A, upper, purple dendrites)—that is, by the expansion of branches along their lengths (Yang and Chien, 2019). Dilation accounts for the growth of the overlying epidermal cells (Parrish et al., 2009) and of class I cells (Castro et al., 2020; Palavalli et al., 2021),

which expand concomitantly with the segments. To test the role of dilation in arbor expansion, we reimaged the same neurons at discrete times over development, at 24 & 48 hr, and at 48 & 96 hr (Figure 2B). As the arbors grow, there is continuous addition and removal of branches. Nevertheless, it was possible to identify shared structural features of proximal, non-terminal branches (branches that lie between two branch points as opposed to terminal branches that end in a tip) (Figure 2 C,D). The fractional increases in lengths of these identified branches were considerably less than the fractional increase in length of the AP and LR segments (Figure 2E), in agreement with earlier measurements (Baltruschat et al., 2020). This finding implies that there must be slow slippage between the class IV cells and the adjacent epidermal cells (Han et al., 2012). Because branch dilation contributes only 3% to 11% of the overall growth of the dendrites, other mechanisms must contribute to the bulk of arbor growth.

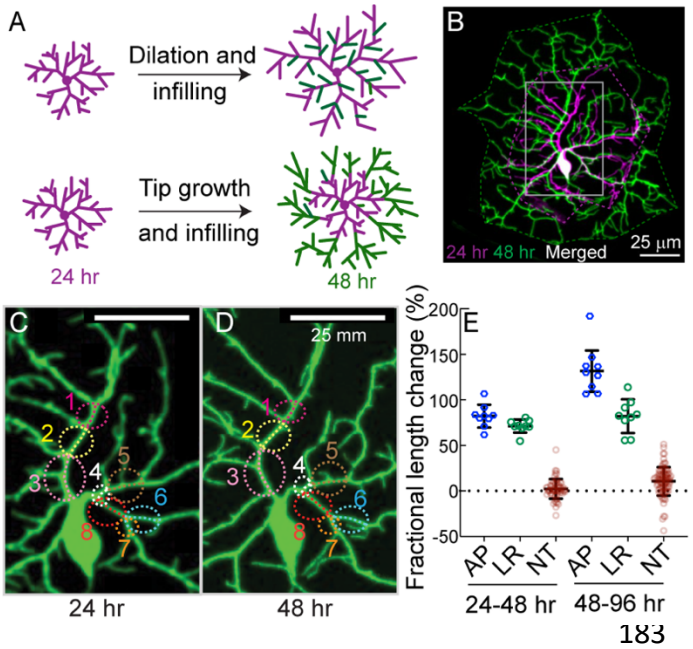

Figure 2. Branch dilation does not account for dendrite growth. A Two models for dendrite growth: dilation & infilling (upper) and branching & tip growth (lower). **B** Maximum-projection image of a GFP-labeled class IV neuron cell at 24 hr (magenta color) and same cell imaged at 48 hr (green color). 24 and 48hr images are combined with a leftward displacement of the latter. **C,D** Conserved non-terminal branches are marked with the same color and number. **E** The fractional length changes from 24 hrs to 48 hrs and from 48 hrs to 96 hrs were calculated for the AP and LR segments, and for the non-terminal (NT) branches (Methods). Each blue and green circle is a different larva; the red circles correspond to several branch measurements in each of 6 larvae.

Terminal dendrites grow from their tips and not from their bases

An alternative hypothesis to dilation is that the growth of the arbor is due to branching and subsequent lengthening of the newly formed terminal branches (Figure 2A, lower). To test this hypothesis, the behavior of terminal dendrites was examined. Following birth by lateral branching from existing branches (Gao et al., 1999), terminal dendrites can: lengthen; shorten spontaneously or following contact with another branch; and

pause (Figure 3A). Time-lapse imaging (Supplementary Movies S1-S5) suggests that lengthening is due primarily to the addition of material near the tip. For example, branch points and bends remain fixed during growth and shortening (Figure 3A, top-left panel; Supplementary Movies S6-10), and the distance between these landmarks and the tips do not change. These observations argue against growth at the proximal end or uniform dilation along the length of terminal dendrites. Because new branches can form as close as 2 μm to an existing tip, we estimate that growth occurs within ~2 μm of the distal ends. Thus, tip growth, which occurs on timescales of minutes, may contribute to the overall growth of the arbor.

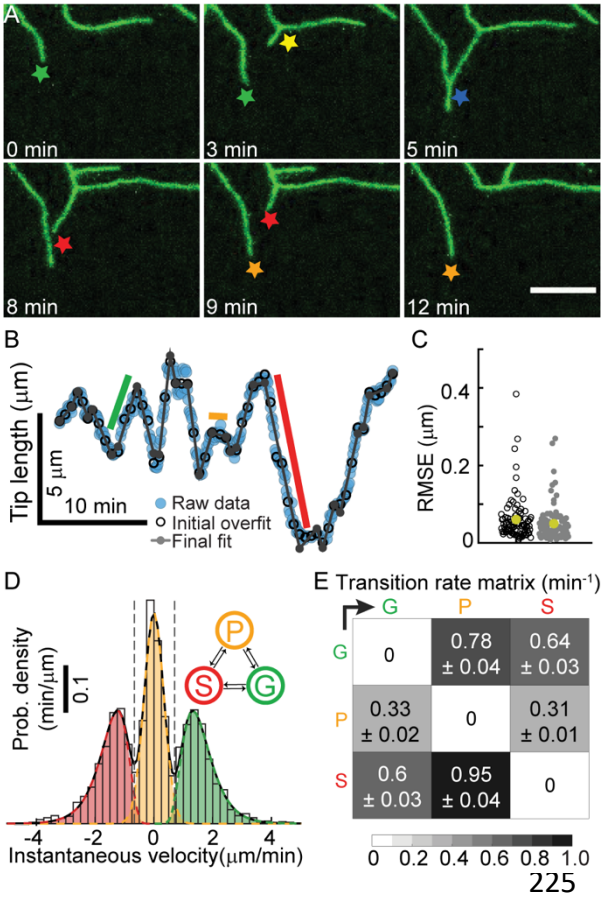

Figure 3. Dendrite tips transition between growing, shrinking and paused states A Class IV dendrites growing (green star), birthing (yellow), colliding (blue), shrinking (red), and pausing (orange). Maximum projection spinning disk images were collected every 5 seconds. **B** The length of a dendrite as a function of time (see Methods). The black open circles represent the initial piecewise linear fit using $N/6$ segments, where N is the total number of frames. The gray dots show the fitting after the iterative merging process (see Methods). Green, orange, and red indicated periods of growth, pausing, and shrinkage. **C** The root-mean-squared error before (black) and after (gray) merging for 91 trajectories (24 hr). The average error is 50 nm. **D** The velocity distribution shows three distinct peaks representing the growing (G), paused (P), and shrinking (S) states. **E** Transition rates between the three states.

High-resolution tracking shows that tips transition between periods of constant growth velocity

To determine whether tip growth can account for arbor expansion, we tracked the lengths of terminal dendrites over time with an accuracy of ~0.1 μm (Methods,

Supplementary Figure 1 A-F). To ensure that mounting and imaging larvae did not interfere with growth, we restricted imaging to 20- to 30-minutes (Supplementary Figure 2A). Typical trajectories show that dendrite growth is highly dynamic, with large fluctuations in velocity (Figure 3B, and Supplementary Figure 1 G, I, K). To analyze tip trajectories, we first considered tip growth as a diffusion-with-drift process, a common way to describe particles moving in a flow. However, we ruled out this description because there were extended times of near-constant velocity: the green, red, and orange lines in Figure 3B (and Supplementary Figure 1G, I, K) clearly indicate periods of elongation, shortening, and stationarity. We therefore fit the trajectories to a piecewise linear continuous function, for which fast algorithms exist (D'Errico, 2021). This initial segmentation into regions of constant velocity provided a good fit to the tracking data (Figure 3B and 3C, black circles), showing that tip trajectories can be decomposed into sequential periods of linear growth or shrinkage.

Dendrite tips undergo dynamic instability

We then asked the more difficult question of whether tips undergo dynamic transitions between growing (G), shrinking (S), and paused (P) states. In other words, can we classify the regions of constant growth into just three states such that transitions only occur between different states. Such a description is analogous to the dynamic instability of microtubules (Mitchison and Kirschner, 1984), which transition stochastically between two states: growing and shrinking.

To test whether a three-state dynamic model could account for tip growth, we assigned each region to be in a growing, shrinking or paused state by fitting the histogram of velocities with a three-peaked distribution, such as shown in Figure 3D, to define velocity thresholds between growth and pause, and shrinkage and pause. We then merged adjacent regions that belonged to the same state. Through an iterative procedure (see Methods), we segmented the trajectories into growing, shrinking, and paused states, with transitions only between different states. The resulting trajectory (Figure 3B, gray lines) was an excellent fit to the data: the root-mean-squared error was on average ~0.05 μm (Figure 3C), accounting for 85% to 99% of the variance (Supplementary Figure 1 H, J, L). From these data, we calculated (i) the growing and

262 shrinking speeds (Figure 3D) and (ii) the rates of the transitions between the three
263 states (Figure 3E). At 24 hr, the growing and shrinking speeds were 1.61 μm/min and
264 1.52 μm/min, respectively, and the rates ranged from 0.31 to 0.95 per minute,
265 corresponding to average lifetimes of individual states between 0.6 to 1.5 minutes. The
266 net speed of dendrite elongation, ~0.034 μm/min (Table 1A), is much smaller than the
267 average speed in the growing state because the dendrites spend roughly equal times in
268 the growing and shrinking states.
269 Thus, the growth trajectories are in accord with a three-state kinetic scheme,
270 which provides a succinct yet comprehensive description of tip dynamics. This scheme
271 is a generalization of the Dogterom and Leibler model of microtubule dynamic instability
272 (Dogterom and Leibler, 1993), with inclusion of a third, paused state, and the growing
273 and shrinking states having distributions of speeds.
274
275 **Dendrite dynamics and branching rates change over development time**
276 Throughout development, the growing and shrinking speeds were roughly unchanged
277 (Table 1A). The main change over development was that the transition rates out of the
278 paused state decreased two- to four-fold and the transition rates into the paused state
279 increased by about 50%. As a result, the dendrites spend more time in the paused
280 state: they become less dynamic.
281 Branching, which always occurs on the sides of existing branches, also slowed
282 down over development. The branching rate per unit dendrite length decreased roughly
283 ten-fold from 24 to 96 hr (Figure 4A, Supplementary Table 1). This decrease is another
284 manifestation of dendrites becoming less dynamic over time. The geometry of
285 branching, however, remained constant over development: the mean angle of a new
286 (daughter) branch was close to 90° at all developmental stages (Figure 4B,
287 Supplementary Table 1), and the spatial distribution of branching remained roughly
288 uniform (Figure 4C and D). In summary, both growth and branching are highly
289 stochastic throughout development, though the transition and branching rates slow
290 down over time.

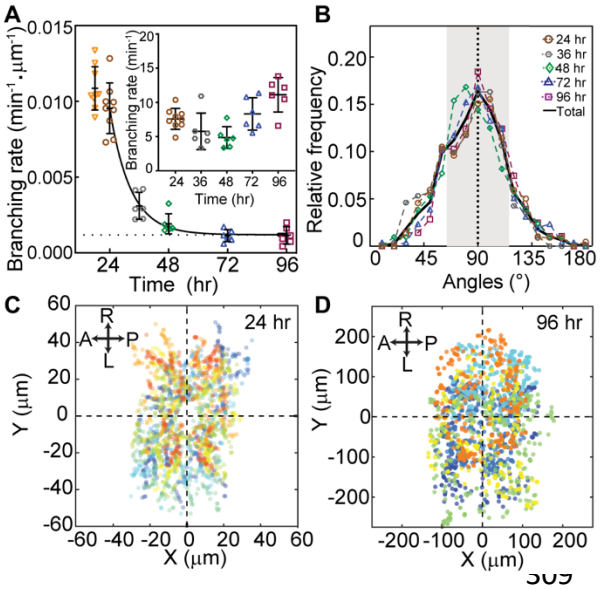

Figure 4. Dendrite branching over development. **A** The rate of appearance of new branches normalized by the total branch length is plotted against developmental time. Each symbol represents a neuron from a different larva (except at 24 hr where 3 neurons in each of 3 larvae were analyzed). The curve is an exponential fit with an offset (dotted line). Inset: The total branching rate per cell. **B** The distribution of branch angles between daughters at different developmental stages. The angle is zero when the new daughter grows parallel to the mother. Numbers of neurons: 6 (24 hr), 7 (36 hr), 4 (48 hr and 96 hr), 5 (72 hr) **C** Spatial distribution of branching events at 24 hr (9 neurons from 3 larvae). **D** Spatial distribution of branching events in 96 hr (6 neurons from 6 larvae). In both **C** and **D**, the soma positions are centered at the origin. Different colors represent different cells.

Dendrite tips retain memories: their dynamics are not Markovian

We tested whether the transitions between growth states are Markovian, meaning that they depend only on their current state: i.e., they do not depend on the history, and there is no memory of earlier states. Consistent with a Markov process, the lifetimes of the states were approximately exponential at long times (Supplementary Figure 3 D-F), and the probability of a transition in the sequence of occupied states (e.g., GPGSPGPSG…) did not depend on the previous state. For example, we found that the likelihood of G→P did not depend on the prior state: that is SG→P and PG→P were equally likely.

There were several violations of the Markov property, however. First, following contact of a tip with another branch, the growth dynamics change: the rates out of the growing state increase, so the dendrites spend less time growing (Table 1B). Therefore, in addition to contact-induced retraction, there is a long-lasting alteration of the dynamics: the average tip-growth rate changes from positive to negative (Table 1), and the post-contact dendrites shrink on average. This alteration implies that there is a long-lasting memory of the collision. Second, we found that the lifetimes of newly born dendrites were longer than expected for a Markov process. Following birth into the growing state, the transition rates, which were measured for older dendrites (>5 minutes after birth), predict that there will be an initial linear decrease in surviving dendrites due

to the chance that a growing dendrite stochastically switches into a shrinking state, which then shortens and disappears. Instead, we found that the survival curve was initially flat, consistent with an initial growing state of 0.3 minutes (Supplementary Figure 4A). Such a survival curve is another violation of the Markov process and implies that a newborn dendrite retains a memory of birth. Third, growth and shrinkage events with higher absolute speeds tended to have shorter lifetimes (Supplementary Figure 3A, B). Branching also showed non-Markovian properties: for example, rebranching occurred more often at points where an earlier dendrite had disappeared (Supplementary Figure 4B, C). Thus, while branching and growth are highly stochastic, they deviate from being Markovian, indicating memory and "hidden variables" that influence the dynamics. These hidden variables are likely to be long-lived biochemical states (e.g., phosphorylation) triggered by dendrite birth or tip contact with other dendrites, which influence the dynamics.

An agent-based model incorporates measured tip properties

To test whether the dynamical properties of the dendrites measured above can account for the observed morphology, we developed an agent-based computational model to predict morphologies based on tip dynamics. The elementary "particle" in the model is the dendrite tip, which serves as the agent (Figure 5A).

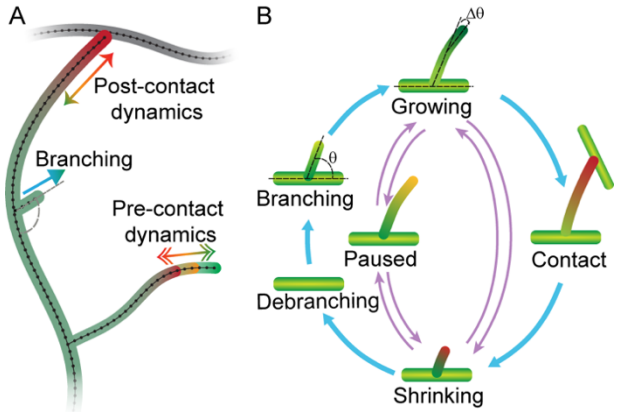

Figure 5: Agent-based computational model A Cartoon diagram depicted the different components of the model: tips are born by branching and transition between growing, shrinking, and paused states. Upon contact with another branch, the tips retract. **B** Diagram of the transitions. Parameters are listed in Table 1 and Supplementary Tables 1-2.

Tips were simulated using rules that closely followed the experimental measurements (see Figure 5B, Methods). Terminal dendrites lengthen and shorten with speeds sampled from the growth and shrinkage distributions (e.g., Figure 3D). They transition between growing, shrinking, and paused states according to the measured transition rates (Table 1), which were linearly interpolated between different developmental stages. Tip birth occurred randomly in time and space along extant branches with the measured branching rates (Figure 4A). The nascent daughter branch was assumed to start in a growing state (Figure 5) with an initial length of $0.5\ \mu\mathrm{m}$ (Supplementary Table 2) and included an initial lag of $0.3\ \mathrm{min}$ during which the transition out of the growing state was forbidden, in accordance with our observations. Dendrite death occurred when the last point disappeared during a shrinkage event. Contact, defined as a tip getting closer than $0.15\ \mu\mathrm{m}$ to another branch (roughly the branch radius (Liao et al., 2021), switched a growing tip to a shrinking one with the post-contact dynamics (Table 1B).

The initial larval morphology at 24 hr was established by (i) growing two to four branches from a point (the origin) using the embryonic growth parameters at (18-20 hr) and (ii) allowing growth until the total branch length and number reached their values at 24 hr. To model the segment boundary, we assumed that contact with neighboring dendrites induced shrinkage (Parrish et al., 2009). Neighbor interaction was implemented using a periodic boundary condition such that one side of a growing neuron feels its opposite side as if growing on the topological equivalent of a torus. Over time, we gradually increased the size of the boundary according to the measured segment growth rates (Figure 1 inset).

Simulated dendritic trees recapitulate coarse-grained features of dendrite morphology

We simulated dendritic trees using the parameters from Table 1 and Supplementary Tables 1,2, all of which were measured or tightly constrained by experiments. The simulations (Figure 6A) recapitulated key properties of real arbors (Figure 6B).

(i) **Tiling:** Simulated arbors tiled the segments, like real arbors. In the absence of a boundary, the widths of simulated arbors initially grew at 10 μm/hr, which is faster

than the segment growth of 4 μm/hour; the simulated arbors, therefore, filled the segments between 48 to 72 hr (Supplementary Figure 5Aii). After that, the simulated arbors grew at 4 μm/hr, just sufficient to keep up with segment growth.

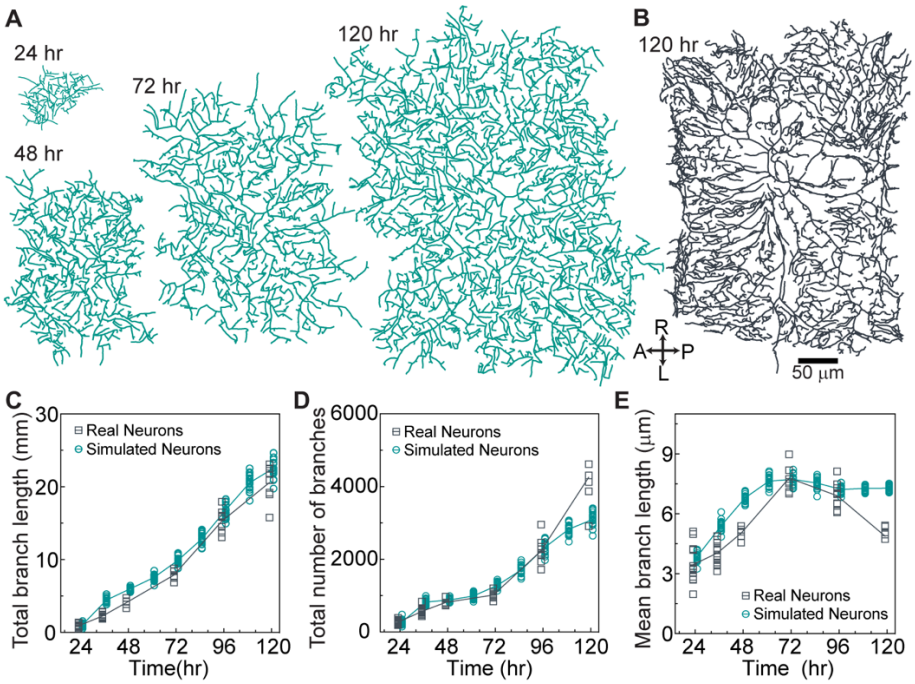

Figure 6. The agent-based model accords with overall neuronal growth A Example of a simulated neuron using the parameters in Table 1 and Supplementary Tables 1-2 at different developmental stages. Same scale bar as in B. **B** Example of the skeleton of a real neuron at 120 hr. **C** Total branch length over developmental for simulated and real neurons. **D** Total number of branches. **E** Mean branch length (total branch length/total number of branches).

(ii) **Total branch length and number**: The simulations predicted the observed increases in total branch length (Figure 6C) and number (Figure 6D), as well as the mean branch length (Figure 6E). The branch length distributions were roughly exponential in the simulations and the data (Supplementary Figure 6 A-E). An interesting feature of the branch number is the initial burst (24-36 hr) and subsequent plateau (36-72 hr). The burst is predicted by the model and arises from two features of tip growth: the high initial branching rate (Figure 4A), and the perseverance of the initial growth of branches (i.e., a delay in transitioning out of the growing state). Without perseverance, which is a memory of birth, the plateau is less pronounced, showing that the initiation of branching is an essential determinant of arbor morphology.

There were some discrepancies between the data and the model. For example, the branch number of the simulated arbors saturated at 120 hr, while that of the real arbors continued to increase with an associated late decrease in mean branch length of real arbors. These discrepancies may indicate that dynamical properties change after 96 hr. Also, the high density at AP boundaries (Figure 6B, right) arises from cell-cell interactions, which we did not include. Nevertheless, we believe that the model is in good agreement with the average properties of the arbors.

Simulated arbors capture the variability of dendrite morphology

In addition to predicting average branch properties, the model also predicted the variation of these features. For example, the measured branch numbers are highly variable, with coefficients of variation (SD/mean, CV) ranging from 0.11 to 0.22 over development. This CV is even larger than that of a Poisson process, a prototypical random process whose CV equals the inverse square root of the branch number (expected range 0.02 to 0.06). This comparison to a Poisson process indicates that branch number is highly variable from arbor to arbor, a manifestation of the stochasticity of the morphology. Total branch length and average branch length were also highly variable. Importantly, the simulations recapitulated this variability (Figure 6C-E). Thus, the model predicted both the average properties and the stochasticity of the branch number and length.

Simulated arbors recapitulate fine-scale properties of dendrite morphology

The branches of both the simulated and real arbors formed dense meshworks (Figure 7A,B). We estimated the extent to which the branches cover the arbor using the box-counting method (Falconer, 1990) in which the number of boxes that contain a branch is plotted against the size of the boxes (Figure 7C). We found that the logarithm of box number was approximately proportional to the logarithm of box size, indicating that the patterns have scale-free and fractal-like properties. The log-linear relation breaks down at box sizes below 5 μm, the size of the “holes” in the pattern due to the average branch size. We defined the fractal dimension as the log-log slope in the central region of the plot encompassing the middle 50% of the points (Figure 7C dashed lines). The fractal

441 dimension increased from 1.4 to 1.8 from 24 hr to 120 hr for both the simulated and real
442 arbors (Figure 7D). Because a region containing a single line has a fractal dimension of
443 1 whereas a region completely filled region has a fractal dimension of 2, the dendritic
444 patterns are of intermediate dimension and at 120 hr nearly fill the plane (fractal
445 dimension 1.8). Though the fractal dimensions of real arbors were consistently lower by
446 about 0.1, we nevertheless conclude that the simulated arbors recapitulate the real
447 arbors in this metric.

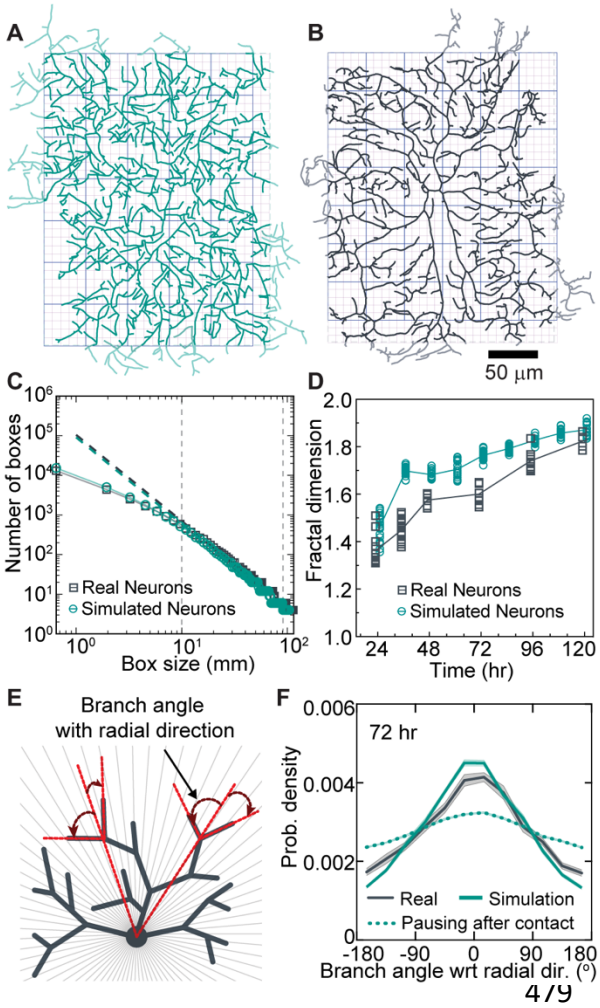

Figure 7. The agent-based model recapitulates the fine-scale patterns of real arbors. A Model arbor at 72 hr. Light green branches indicate the outer 5% of the arbors excluded from the analysis to mitigate against spurious boundary effects (see Methods). Boxes with two different sizes are shown in the background. **B** Skeletonized real arbor at 72 hr. Light gray branches were excluded from the analysis. **C** The number of boxes that contain a branch (*y*-axis) is plotted against the box size (*x*-axis). The slopes over the central 50% of the data (vertical dashed lines) define the fractal dimensions. **D** Fractal dimensions of real and simulated arbors both increase over developmental. **E** Diagram defining the radial orientation. **F** Radial orientation of a simulated tree (green solid line) and a real arbor (black) at 72 hr. Simulated tree with pausing instead of retraction (green dotted curve).

479

480

481 **Simulations predict the radial orientation of dendrite branches**

482 We discovered that class-IV cells have an unexpected long-range order: branches are
483 not randomly oriented but instead tended to be parallel to the radial orientation (Figure
484 7E-F, Supplementary Figure 6 F-J). The simulations also displayed radial orientation.
485 Radial orientation is a consequence of contact-based retraction; if contact-based

retraction is replaced by contact-based pausing, the radial orientation was greatly reduced (Figure 7F, dotted curve).

Discussion

We have discovered that the tips of *Drosophila* class IV dendrites transition stochastically between three states - growing, shrinking, and paused. This allows dendrites to explore extracellular space, analogous to the exploration of intracellular space by microtubules undergoing dynamic instability (Kirschner and Mitchison, 1986). Our modeling shows that these transitions, together with lateral branching, and contact-mediated retraction, give rise to the complex and highly variable morphology of the dendritic arbors, allowing them to fulfill their biological functions. The dense, almost unbroken meshwork optimizes detection of the fine ovipositor barbs of parasite wasps (Basak et al., 2021; Robertson et al., 2013). And the radial orientation of branches, a form of long-range order that emerges from local interactions (Toner and Tu, 1995; Vicsek et al., 1995), namely contact-induced retraction, reduces the path distance to the cell body: this minimizes signaling delays and wiring costs (Baltruschat et al., 2020). Thus, stochastic tip dynamics may partially solve the riddle of how “the morphological features displayed by neurons appear to obey precise rules that are accompanied by useful consequences” (Cajal, 1995).

Dendrite tips: an intermediate organizational principle of dendrite morphology

Our results strongly support the concept that the dendrite tip is a “branching engine … that initiates, directs, and maintains branch outgrowth during development and regrowth” (Lu and Werb, 2008). The dendrite tip, with a diameter of only 0.2 μm (Liao et al., 2021) and with dynamics on the timescale of ~1 minute (the state lifetimes), generates structures up to 500 μm in diameter (>1000-times larger sizes) over five days (>1000-times longer times). Tips, therefore, are intermediate in length- and timescales between molecules and morphology.

The concept of the dendrite tip as a branching machine has four important implications. First, if the molecular basis of tip growth and branching can be elucidated, our agent-based model will provide a full connection between genotype and phenotype,

518 with the caveats that morphogenesis is stochastic and some features such as three
519 dimensionality are not included. Second, altered tip dynamics due to mutations and
520 diseases may underly altered dendrite morphologies (see Introduction and the
521 Predictions of the model section). Third, tip rules may specify neuronal identity, often
522 defined by dendrite morphology (DeFelipe et al., 2013). And fourth, the stochastic
523 nature of the tip rules may facilitate the evolution of neuronal cell types. This is because
524 developmental stochasticity amplifies genetic variation by allowing a large class of
525 morphologies to be sampled for each genotype. While some morphological outliers may
526 function poorly, others might be beneficial, and genetic and/or epigenetic mechanisms
527 could selectively stabilize these beneficial morphologies.
528
529 **Potential molecular mechanisms underlying dendrite tip dynamics and branching**
530 Neurite elongation by tip growth also occurs in axons (Dent et al., 2011) and in other
531 dendrites, such as those in *C. elegans* PVD neurons (Liang et al., 2020). An important
532 difference between dendrite tips in class IV cells and the growth cones seen in these
533 other cells is that the tips of class IV dendrites are much smaller. The diameter of class
534 IV terminal dendrites is only ~200 nm (Liao et al., 2021), as small as a single filopodium,
535 the finest feature of growth cones observed under the light microscope. Thus, tip-growth
536 mechanisms in class IV dendrites likely differ from growth-cone-based growth. An
537 important open question is how the cytoskeleton and membranes reach the dendrite
538 tips: what are the relative contributions of diffusion, filament polymerization (Delandre et
539 al., 2016; Jinushi-Nakao et al., 2007; Nithianandam and Chien, 2018; Ori-McKenney et
540 al., 2012; Sears and Broihier, 2016; Yalgin et al., 2015), motor-driven transport (Arthur
541 et al., 2015; Weiner et al., 2016) and motor-driven sliding (Winding et al., 2016)?
542
543 **Morphological predictions of the model**
544 The agent-based model allowed us to explore which parameters are important for arbor
545 growth and mesh size (Supplementary Figure 5) and provides hypothesis for the
546 phenotypes of mutants.
547 A surprising finding was that branching drives overall arbor growth: increasing
548 the branching rate not only increased the number and density of branches, as expected,

549 but also increased arbor size. Indeed, setting the average velocity of dendrite extension
550 to zero still resulted in arbor growth, albeit slower, showing that branching without net tip
551 growth can drive arbor expansion. The modeling showed that increasing the fluctuations
552 in branch length (by reducing the tip-transition rates) also increased the growth rate.
553 This suggests an unexpected growth mechanism: length fluctuations are locked in by
554 the formation of new branches. The branching angle also affected arbor growth: if the
555 branch angle was decreased to 45° (i.e., growth towards the direction of the mother
556 branch), arbor growth increased, showing that outward growing branches are more
557 likely to survive. The persistence of branch growth after birth was also important.
558 Therefore, branching is essential not just for infilling the network but also for expansion.
559 Our model shows dendrite density is set by the interplay between branching and
560 self-avoidance, which acts as negative feedback. Inhibition of self-avoidance increases
561 the branch density as observed by several mutation studies (Emoto et al., 2004;
562 Hughes et al., 2007; Matthews et al., 2007; Soba et al., 2007). By allowing the dendrite
563 tips to ignore contact-based retraction with the neighboring branches, our model
564 produced high density of branches (see Supplementary Table 3).
565 Our observation that branching is an intensive property—the total rate of
566 formation of branches is almost independent of arbor size (Figure 4A, inset)—is
567 evidence that there are only a limited number of “branching factors” being produced in
568 the entire cell per unit time. The uniform distribution of new branches suggests that the
569 branching factors are dispersed throughout the cells, perhaps by molecular motors.
570 Several phenotypes of molecular motor mutants in class IV cells support this
571 hypothesis. The perturbation of molecular motors and their adapter proteins, including
572 dynein (Arthur et al., 2015; Satoh et al., 2008; Zheng et al., 2008) and kinesins (Kelliher
573 et al., 2018; Satoh et al., 2008), result in non-uniform branch densities, as expected if
574 the distribution of branching factors were disrupted (see Supplementary Table 3).
575 The transition rates between growth states are also important. For example, the
576 dendrite tips of Katanin (Kat-60L1) mutants spend less time in the paused states and
577 more time in the shrinking states compared to controls (Stewart et al., 2012). Our
578 simulations recapitulated the sparser morphologies reported in Stewart et al. (see
579 Supplementary Table 3).

General mechanisms of branching morphogenesis

Dendrite tips share features of branch tips in other systems. Tip cells drive branching in branched tissues such as the mammary glands (Lu and Werb, 2008). The growing ends of cytoskeletal filaments, with associated nucleation factors, drive branching of organelles such as the microtubule-based mitotic spindle (Decker et al., 2018; Petry et al., 2013) and the actin-based lamellipodium (Pollard and Borisy, 2003). In all three cases (dendrites, tissues and cytoskeleton), the tips operate at shorter length-scales and timescales than those of the structures they produce. Furthermore, they all respond to external signals: contact-based retraction of dendrite tips, cortex-induced catastrophe of microtubule ends (Komarova et al., 2002), and self-avoidance of mammary-gland branches (Lu and Werb, 2008). Finally, all three are stochastic and generate highly variable morphologies. Given these commonalities, it is likely that the principles that we have elucidated for dendrites generalize to other branched systems.

Acknowledgments

We thank all members of the Howard lab for many helpful discussions and suggestions. Special thanks to Dr. Ashley Arthur for proofreading the manuscript. We thank Hermann Cuntz, Damon Clark, and John Carlson for comments on an earlier version of the manuscript, and Chun Han and the Bloomington Drosophila Stock Center for fly stocks. O.T. was supported by the Fonds de Recherché du Quebec - Nature et Technologies; X.L. was supported by the National Natural Science Foundation of China (NSFC Grant 31671389, to X.L.) and the Max-Planck Partner Program; and J.H. was supported by NIH grants DP1 MH110065 and R01 NS118884.

Author Contributions

SSh, SSu and JH designed the experiments based on early results by XL. SSh conducted the experiments and analyzed branching. SSu, OT, YT and JH conceptualized the models, which were implemented by SSu, who performed image and tip tracking analysis and wrote the source code for the *in-silico* model, based on earlier work by OT. SSh, SSu and JH wrote the manuscript.

Declaration of Interests

The authors declare no competing interests.

Table 1

A: Pre-contact tip-dynamics parameters

Age (hr)	Tip velocity parameters			Tip transition rates						Corr.	Average tip velocity	
	μ_G, σ_G (μm/min)	μ_P, σ_P (μm/min)	μ_S, σ_S (μm/min)	k_{GP} (min^{-1})	k_{GS} (min^{-1})	k_{PG} (min^{-1})	k_{PS} (min^{-1})	k_{SG} (min^{-1})	k_{SP} (min^{-1})	*r* & *p*	v_d^{Tracks} (μm/min)	$v_d^{TranMat}$ (μm/min)
18-20 (E)	0.37, 0.34 $V_G = 1.53$	0, 0.36	0.43, 0.37 $V_S = 1.65$	0.696	0.509	0.423	0.296	0.669	0.71	0.017 0.09	0.097 ±0.0158	0.100 ±0.0151
24 (L1)	0.41, 0.36 $V_G = 1.61$	0, 0.34	0.35, 0.37 $V_S = 1.52$	0.784	0.64	0.335	0.314	0.598	0.946	0.008 0.65	0.034 ±0.0196	0.038 ±0.0191
48 (L2)	0.40, 0.39 $V_G = 1.61$	0, 0.25	0.0, 0.41 $V_S = 1.1$	0.933	0.435	0.155	0.235	0.282	1.251	0.045 0.24	0.020 ±0.1545	0.026 ±0.0177
96 (L3)	0.36, 0.52 $V_G = 1.64$	0, 0.25	0.19, 0.44 $V_S = 1.33$	0.923	0.799	0.116	0.117	0.575	1.276	0.002 0.9	0.008 ±0.0039	0.022 ±0.0177

B: Post-contact tip-dynamics parameters

Age (hr)	Tip velocity parameters			Tip transition rates						Corr	Average tip velocity	
	μ_G^*, σ_G^* (μm/min)	μ_P^*, σ_P^* (μm/min)	μ_S^*, σ_S^* (μm/min)	k_{GP}^* (min^{-1})	k_{GS}^* (min^{-1})	k_{PG}^* (min^{-1})	k_{PS}^* (min^{-1})	k_{SG}^* (min^{-1})	k_{SP}^* (min^{-1})	r & p	v_d^{Tracks} (μm/min)	$v_d^{TranMat}$ (μm/min)
18-20 (E)	0.53, 0.49 $V_G^* = 1.9$	0, 0.28	0.53, 0.54 $V_S^* = 1.9$	0.635	0.992	0.263	0.401	0.469	0.593	0.07 0.12	-0.42 ±0.07	-0.34 ±0.07
48 (L2)	0.40, 0.50 $V_G^* = 1.7$	0, 0.25	0, 0.38 $V_S^* = 1.1$	1.446	1.24	0.134	0.29	0.239	0.814	0.018 0.76	-0.23 ±0.05	-0.19 ±0.04

Errors are SE.

Methods

Fly Stocks and maintenance

The fly line *ppk-cd4-tdGFP* was used to image class IV dendritic arborization neurons and was a kind gift from Dr. Han Chun (Cornell University). Fly crosses were maintained in fly chambers at 25 °C, 60% humidity in a Darwin Chamber with 12 -hour light/dark cycles. An apple-agar plate was used to collect the fly embryos and a big drop of yeast paste was put in the center of the agar plate to induce egg-laying.

Apple-agar plates were made by mixing 4X apple juice concentrate (355 ml), water (300 ml), dextrose (155 gm), sucrose (80 g). This solution was stirred and heated to dissolve the sugars, and agar (Bacto agar, Becton Dickinson, 60 g) and 1.25N NaOH (70 ml) were added. The solution was covered loosely with foil and autoclaved in the liquid cycle for 30 min. The plating mixture contained 100 ml of this apple-agar concentrate, 197 ml of water, and 3 ml of Acid mix A—an equal mixture of propionic acid (100%, 83.6 ml, and 16.4 ml water) and phosphoric acid (100%, 8.3 ml and 91.7 ml water).

For neuron morphometrics, embryos were collected every 15 minutes and imaged when they reached the appropriate age **A**fter **E**gg **L**ay (AEL): 24hr, 48hr, 72hr, 96hr, and 120hr.

Sample preparation

For imaging, embryos of appropriate age (18 hr to 22 hr AEL) were collected from apple-agar plates and dechorionated by gently rolling them on a piece of double-sided tape stuck to a glass slide. The dechorionated embryos were then placed with their dorsal side down on a No. 1.5 coverslip, MatTex, with a small drop of halocarbon oil 700. A piece of wet Kim wipe was placed near the embryos to maintain humidity during imaging. No anesthetics were used for embryo imaging. For larvae imaging, larvae of ages 24 hr, 48 hr, 72 hr, 96 hr, and 120 hr were washed with 20% and 5% sucrose solution, anesthetized using FlyNap (Carolina Biologicals, Burlington, NC, USA), and transferred to apple-agar plates to recover for 1-5 minutes. After recovery, larvae were gently placed with their dorsal side up on a 1% agar bed adhered to a glass slide and imaged in a drop of 50% PBS, 50% Halocarbon oil 700 (Sigma Aldrich). Larvae were further immobilized by gently pressing them with a 22mm X 22mm coverslip lined with Vaseline or vacuum grease.

Imaging

Samples were imaged on a spinning disk microscope: a Yokogawa CSU-W1 disk (pinhole size 50 µm) built on a fully automated Nikon TI inverted microscope with perfect focus, 488nm laser illumination at 18-21 % laser power, either a 40X (1.25 NA, 0.1615-micron pixel size) or a 60X (1.20 NA, 0.106-micron pixel size) water immersion objective, an sCMOS camera (Zyla 4.2 plus), and Nikon Elements software. The temperature of the sample region was maintained using an objective space heater at 25°C (OKO labs stage heater). Samples were manually focused to identify abdominal third and fourth segments (A3 or A4 neurons) before image acquisition. Full-frame movies (2048×2048 pixels) containing 6 to 12 1-µm sections were collected every 4-6 s. Static images for morphometric studies were acquired using a 60X water immersion

objective for 24 hr and 40X objective for later stages. Images were stitched using in-house code (https://github.com/oliviertrottier/neuron-stitch). Movies were curated for subsequent offline analysis. Image analysis (segmentation, skeletonization, branching analysis, and angle measurements) was done using ImageJ.

Controls for growth

Class IV neurons are susceptible to mechanical pressure, which, if too large, stops growth and causes degeneration. Therefore, embryos were imaged without an overlying coverslip. Larvae were immobilized with minimal pressure under a coverslip and were placed on a 1% agar bed. As a control, we plotted the size of neurons throughout imaging to confirm that they remain on the "standard" growth curve (Supplementary Figure 2 A).

Segment length determination

The *Drosophila* larval abdomen is divided into eight segments (Supplementary Figure 2 B). Each segment on the dorsal side has two neurons, each occupying a hemi-segment. Each hemi-segment is approximately rectangular with Anterior-Posterior (AP) and Left-Right (LR) axes. The AP length was measured as the distance between the cell bodies of the adjacent neurons on the anterior and posterior sides. The LR length was measured as the distance between cell bodies in adjacent hemi-segments (across the midline) corrected for the offset of the cell bodies, which are not in the centers of the cells but displaced away from the midline. The AP and LR segment lengths were measured for three larvae for all the respective stages.

Arbor skeletonization

Images were maximally projected and individual dendrites manually segmented from their neighbors. The segmented neurons were binarized using custom made algorithm and skeletonized using MATLAB's '`bwmorph`'. The identified branch points are then subtracted from the skeleton to generate isolated individual branches.

Branch length measurements

The pixel coordinates of all the branches were smoothed using a spline to calculate the total length of all branches and their average length.

Dendrite arbor width

Arbors are approximately rectangular. If the mass of the dendrite skeleton is uniformly distributed in a rectangle, then the widths, D_{AP} and D_{LR}, are:

$$D_{\mathrm{AP}} = \sqrt{12}\, R_{\mathrm{g}}^{\mathrm{AP}} \quad \text{and} \quad D_{\mathrm{LR}} = \sqrt{12}\, R_{\mathrm{g}}^{\mathrm{LR}}$$

where R_{g} is the radius of gyration defined by:

$R_{\mathrm{g}} = \sqrt{\frac{1}{N}\sum_{j=1}^{N}\left(r_j - \bar{r}\right)^2}$ where N is the total number of occupied pixels in the skeleton, r_j is the projection onto the respective axis of the jth occupied pixel and $\bar{r}$ is the mean projected position of all occupied pixels. R_{g} is the standard deviation of the dendrite pixels i.e., their spread from the center. We confirmed that the widths defined in this way were good approximations to the 95% rectangles containing 95% of the skeletal mass.

Dilation analysis

To study the possible role of dilation in arbor growth, we imaged the same dorsal neurons (A3, A4, and A5) every 24 hrs. Larvae were mounted and imaged as described but without the use of anesthetics. Their movement was minimized by imaging at 4 °C for 2-5 mins. They were then returned to the apple-agar plate in the Darwin Chamber. The larvae were imaged using 20X and 40X objectives. For image analysis, the same neurons at 24 & 48 hr, and 48 & 96hr were segmented and aligned using ImageJ to identify conserved branches. These branches were proximal and non-terminal. The fractional increase in branches and segment lengths were defined as

$$\text{Fractional length change (\%)} = \frac{\text{Final length} - \text{Initial length}}{\text{Initial length}}$$

Branching rate and branch angle

To determine branching events, time-lapse movies of duration 20-30 minutes were analyzed manually using ImageJ. A new protrusion of length >0.25 μm was scored as a new branch. The total branching rate (min^{-1}) was calculated by dividing the total number of branching events by the total time. The specific branching rate ($\mu\text{m}^{-1}\text{min}^{-1}$) was calculated as the total branching rate divided by the total branch length. The spatial distribution of all branching events was plotted using MATLAB with the soma at the origin $(x = 0, y = 0)$. The angle of new branches was measured using the angle tool of ImageJ (zero angle defined as in the direction of the mother). The angle distribution graph was plotted using Prism.

Fractal Dimension

We used the box-counting method to calculate the fractal dimension. For each box width, W, we measured the number of boxes, $N(W)$, needed to cover all the occupied pixels of the skeleton (Figure 7A). $N(W)$ is approximately linear on a log-log plot (Figure 7C) indicative of a power law. The middle 50% of points (between the dashed lines in Figure 7C) was fit to $N(W) = W^{-D_\mathrm{f}}$ to obtain the fractal dimension D_f.

Tip-tracking algorithm

To quantify the dynamical properties of the tips, we developed an in-house algorithm to track dendritic tips and determine dendrite length-time curves. Time-lapse movies were stabilized, maximum-projected (ImageJ), and terminal dendrites selected for analysis based on their separation from neighboring dendrites and the signal-to-background ratio. Terminal dendrites were selected throughout the arbor. Examples are shown in Figure 3 A. Extraneous objects were manually deleted.

To track the growing and shrinking tips, the algorithm determined the longitudinal centerline of the terminal dendrite and the location of its end for each frame. The central line was computed by fitting Gaussians to the cross-sectional intensity profiles at regular intervals along the backbone of the dendrite using:

$$I(x) = I_0\, e^{\frac{-(x - x_\mathrm{c})^2}{2\sigma^2}} + d$$

(Demchouk et al., 2011) where x is the position along a normal to the dendrite, I_0 is the peak intensity value, x_c is the center of the Gaussian, σ is the standard deviation and d

752 is the measured camera offset (100) plus the background fluorescence. To compute the
753 location of the tip, $(x_{\text{tip}}, y_{\text{tip}})$, we fit a 2-dimensional Gaussian function convolved with
754 an error function using (Demchouk et al., 2011):

755 $$I(x,y) = I_0 \exp\left[\frac{-\left[(y - y_{\text{tip}})cos\theta - (x - x_{\text{tip}})sin\theta\right]^2}{2{\sigma_v}^2}\right] \cdot \operatorname{erfc}\left[\frac{(y - y_{\text{tip}})cos\theta - (x - x_{\text{tip}})sin\theta}{\sigma_p}\right] + d$$

756 where I_0 is the peak intensity, θ is the angular direction of the tip, and σ_v and σ_p are the
757 standard deviations along the orthogonal and parallel directions. The length of the
758 dendrite in each frame was determined by fitting the center line and the tip with a cubic
759 spline. Length-time traces were smoothed with a median filter of size 3 to remove
760 glitches.
761 To estimate the precision of our tracking algorithm, we used two different
762 approaches. In the first, we tracked synthetic images of capped cylindrical tubes of
763 known length and radius with fluorophores placed randomly on their surfaces (10%
764 labeling density) and convolved with a point spread function (350 nm FWHM). To
765 ensure that our algorithm could perform robustly under a wide range of signal-to-
766 background ratios, we tested the tracking accuracy with decreasing signal to
767 background ratios. The typical precision was $\ll$1 pixel (100 nm) even for low signal-to-
768 background ratios (Ruhnow et al., 2011). (ii) We tracked the position of *in-vivo* dendritic
769 tips that are in long-term paused states and found that the average standard deviation
770 of length was ~0.1 μm (< 1 pixel, 0.1615 μm) as shown in Supplementary Figure 1 D.
771 This accuracy is comparable to and, in some cases, better than available software, such
772 as, FIESTA (Ruhnow et al., 2011), JFilament (Smith et al., 2010), and Simple Neurite
773 Tracer (Longair et al., 2011). Using a parallelized method, several hundred tips can be
774 tracked simultaneously. A caveat of our method is that it can only track filaments that
775 are reasonably free of extraneous objects, excessive noise, and have no breaks,
776 discontinuities, or overlapping segments.
777
778 ***Calculating velocities and transition rates***
779 Fitting piecewise linear functions to the data is an ill-posed problem (Hansen and
780 O'Leary, 1993) because a perfect fit can always be achieved with a large enough
781 number of segments (equal to the number of data points minus one). To circumvent this
782 problem, we defined a temporal resolution, *T* (in frames), that is necessary to
783 distinguish a transition event from the noise in the data. Then, the maximum number of
784 segments in each trajectory was calculated by dividing the total number of data points
785 (total number of frames) by the temporal resolution. We used simulated data to estimate
786 the temporal resolution that performs the best. We generated Markovian trajectories
787 with known and realistic velocity distribution (±1.5 μm/min) and transition rates (0.5 min^{-}
788 ^{1}), similar to those shown the Figure 3. We then, added Gaussian white noise of
789 standard deviation 0.25 μm to the trajectories to mimic the experimental noise. To
790 analyze the trajectories, we used the following steps as shown in Supplementary Figure
791 7:
792 (i) We fit the trajectories with piecewise linear function considering N_{data}/T as the initial
793 number of segments (N_{seg}).
794 (ii) The velocity distribution (slope of the segments) was fitted to a lognormal-Gaussian-
795 lognormal distribution:

$$v_T = \frac{1 - C_{\mathrm{G}} - C_{\mathrm{S}}}{\sqrt{\{2\pi\sigma_{\mathrm{P}}^2\}}} e^{\left\{-\frac{(v-\mu_{\mathrm{P}})^2}{2\sigma_{\mathrm{P}}^2}\right\}} + (v > 0)\frac{C_{\mathrm{G}}}{v\sqrt{\{2\pi\sigma_{\mathrm{G}}^2\}}} e^{\left\{\frac{(\log(v)-\mu_{\mathrm{G}})^2}{2\sigma_{\mathrm{G}}^2}\right\}} + (v < 0)\frac{C_{\mathrm{S}}}{|v|\sqrt{\{2\pi\,\sigma_{\mathrm{S}}^2\}}} e^{\left\{-\frac{(\log|v|-\mu_{\mathrm{S}})^2}{2\sigma_{\mathrm{S}}^2}\right\}}$$

where the C's are the normalization constants, the μ's are the means, the σ's are the standard deviations and the subscripts $\mathrm{P}, \mathrm{G}, \mathrm{S}$ stand for paused, growth, and shrinkage states respectively. The first term is a Gaussian and denotes the paused state, whereas 2nd and 3rd terms are log-normal distributions representing the growth and shrinkage states.

After fitting the above velocity distribution, the intersections between the paused and growth distribution (I_{G}) and the paused and shrinkage distribution (I_{S}) were calculated, and the segments labeled using these two velocity thresholds.

(iii) Consecutive segments with similar labels were then merged. This process decreased the number of segments ($N^{\mathrm{n}}_{\mathrm{seg}}$). The trajectories were then refitted with the new number of segments. Steps (ii) and (iii) were repeated until $N^{\mathrm{n}}_{\mathrm{seg}}$ stabilized.

(iv) Finally, the transition rates were calculated by counting the total number of transitions from one state to another and then dividing that number by the total time spent in that state. For example, if N_{GP} is the total number of transitions from G to P state and T_{G} is the total time spent in the G state, then the transition rate from G to P is $K_{\mathrm{GP}} = \frac{N_{\mathrm{GP}}}{T_{\mathrm{G}}}$.

Supplementary Figure 7 shows the working protocol along with the validation of our analysis method. To estimate the optimal frame resolution, we plotted the root-mean-squared difference between the input and output transition rates as a function of the frame resolution. Our analysis clearly shows that temporal resolution of 6 frames generates the best results for rates ~0.5/min and noise ~0.25 μm. We used this frame resolution for all our tip dynamics data analysis.

Average tip velocity & validation of segmentation

The segmentation yields a set of intervals, i, with associated distances, d_i, durations, t_i and velocities, $v_i = d_i/t_i$. The distribution of velocities is fit to a lognormal-Gaussian-lognormal model $p(v)$ with parameters $P_{\mathrm{G}}, \mu_{\mathrm{G}}, \sigma_{\mathrm{G}}, P_{\mathrm{P}}, 0, \sigma_{\mathrm{P}}, P_{\mathrm{S}}, \mu_{\mathrm{S}}, \sigma_{\mathrm{S}}$ such that

$$1 = \int p(v)dv = P_{\mathrm{G}} + P_{\mathrm{P}} + P_{\mathrm{S}} \quad (1)$$

and

$$\int L_{\mu_G,\sigma_G}(v)dv = \int L_{\mu_S,\sigma_S}(v)dv = \int G_{0,\sigma_P}(v)dv = 1 \quad (2)$$

where $L_{\mu_G,\sigma_G}(v)$ and $L_{\mu_S,\sigma_S}(v)$ are the log-normal distributions corresponding to growth and shrinkage and $G_{0,\sigma_P}(v)$ is the Gaussian distribution of the paused state. Transitions can only occur between unlike states. This imposes an important structure on the data: there are two threshold velocities v_+ and v_- such that if the segment velocity $v_i > v_+$ then it is assigned to be a growing segment. Likewise, if $v_i < v_-$ it is a shrinking segment. The ones in the middle are paused.

The average velocity as:

$$v_d \equiv \frac{\sum_i d_i}{\sum_i t_i} = \frac{\sum_i v_i t_i}{\sum_i t_i} = \frac{n\bar{v}\bar{t} + n r_{v,t}\sigma_v\sigma_t}{n\bar{t}} = \bar{v} + r_{v,t}\sigma_v\frac{\sigma_t}{\bar{t}} \quad (3)$$

where $\bar{v}$ is the mean velocity, $\bar{t}$ is the mean time, and $r_{v,t}$ is the Pearson correlation coefficient. We used the definition of the Pearson's correlation coefficient $r_{x,y} = \sigma_{x,y}/\sigma_x\sigma_y$ and cross-correlation $\sigma_{x,y} = \left(\frac{1}{n}\right)\sum_i x_i y_i - \bar{x}\bar{y}$ to calculate equation 3. The average velocity v_d has two parts: $\bar{v}$, calculated assuming t_i and v_i are independent of each other, and a cross-correlation term, $r_{v,t}\sigma_v \frac{\sigma_t}{\bar{t}}$. $\bar{v}$ is given by:

$$\bar{v} = P_G \cdot \bar{V}_G + P_s \cdot \bar{V}_S \tag{4}$$

where $\bar{V}_G$ and $\bar{V}_S$ are the first moments of the lognormal velocity distributions for growth and paused states, and P_G and P_s can be calculated from the master equation associated with the transition matrix:

$$\frac{dP_G(t)}{dt} = -(K_{GP} + K_{GS})P_G(t) + K_{PG}\, P(t) + K_{SG}\, P_s(t) \tag{5}$$

$$\frac{dP_P(t)}{dt} = K_{GP}\, P_G(t) - (K_{PG} + K_{PS})\, P_P(t) + K_{SP}P_s(t) \tag{6}$$

$$\frac{dP_s(t)}{dt} = K_{GS}\, P_G(t) + K_{PS}\, P_P(t) - (K_{SG} + K_{SP})P_s(t) \tag{7}$$

where $K_{ij,j\neq i}$ $i,j = \{G,P,S\}$ are the transition rates. The steady state solution, assuming $\frac{dP_G(t)}{dt} = \frac{dP_P(t)}{dt} = \frac{dP_s(t)}{dt} = 0$ and using equation 1, is:

$$P_G = \frac{K_{PG} * K_{SG} + K_{PG} * K_{SP} + K_{PS} * K_{SG}}{D} \tag{8}$$

$$P_P = \frac{K_{GP} * K_{SG} + K_{GP} * K_{SP} + K_{GS} * K_{SP}}{D} \tag{9}$$

$$P_s = \frac{K_{GS} * K_{PG} + K_{GP} * K_{PS} + K_{GS} * K_{PS}}{D} \tag{10}$$

where
$D = K_{GS} \cdot K_{PG} + K_{GP} \cdot K_{PS} + K_{GS} \cdot K_{PS} + K_{GP} \cdot K_{SG} + K_{GP} \cdot K_{SP} + K_{GS} \cdot K_{SP} + K_{PG} \cdot K_{SG} + K_{PG} \cdot K_{SP} + K_{PS} \cdot K_{SG}$.

Finally, the average velocity as:

$$v_d = P_G \cdot \bar{V}_G + P_P.\bar{V}_P + P_s \cdot \bar{V}_S + r_{v,t}\sigma_v \frac{\sigma_t}{\bar{t}} \tag{11}$$

The average velocity is a key parameter, which controls the growth of the simulated arbor (Supplementary Figure 5 D & E). The average velocity calculated in this way from the transition matrix agreed with that calculated directly from the raw traces at all developmental stages (Table 1) considering the Pearson correlation coefficient $r_{v,t} = 0$ (Supplementary Figure 3 C) This validates of our segmentation scheme.

Computational model:

The agent-based two-dimensional computational model of dendritic growth incorporated the fundamental processes that govern the morphogenesis of Class IV neurons: (i)

branching, (ii) tip dynamics, and (iii) contact-based retraction (non-overlapping). We started our simulation with randomly oriented 2-4 branches emanating from the origin (cell body). Each branch is a filament, and points (x, y) are added at 0.1 μm (Δl) intervals as the branch grows. The simulation is divided into 0.1-minute time steps (Δt). The details of individual processes are as follows:

Branching:

Assuming the branching is a random process, we visit all the branches randomly and calculated the branching probability $P_b = 1 - e^{-L_b \omega_b \Delta t}$, where L_b is the length of the branch and $\omega_b$is the branching rate per unit time per unit length (Figure 4A). Then, a uniformly distributed unit random number $R(0,1)$ is compared to P_b to spawn a nascent branch from a random point on the mother branch. The branching angle is chosen randomly from the measured branch angle distribution which is distributed normally with a mean ~90° and standard deviation ~26° as shown in Figure 4B and Supplementary Table 1. Each newly spawned branch is assumed to start in the growing phase with an initial length of 0.5 μm.

Tip Dynamics:

Each branch with a free end (tip) follows a Markov process (after an initial lag, see below), transitioning between growing (G), paused (P), and shrinking (S) states with measured transition rates ($K_{ij, j \neq i}$ $i, j = \{G, P, S\}$;) and velocities ($V_{\{G,P,S\}}$) for free tips (Figure 3H-J). The transition dynamics is implemented using a standard 'Monte-Carlo' method. At each time step, the total probability of transition is calculated using $P_i = 1 - e^{-K_{tot} \Delta t}$, where K_{tot} is the sum of the transition rates from one particular state: $K_{tot} = \sum_{j=\{G,P,S\}}^{j \neq i} K_{ij}$. For example, the total transition rate from the growth state is $K_{tot} = K_{GP} + K_{GS}$. Subsequently, P_i is compared with a uniform random number $R(0,1)$ to implement the transition. If there is a transition, it happens maintaining the ratio K_{ij}/K_{tot}. After the transition, the tip is assigned with corresponding state velocity, the magnitude of which is randomly chosen from their respective velocity distributions (lognormal for growth and shrinkage and normal for paused) (Figure 3). The growth process is implemented by adding new points to the existing branch tip at each time step, Δt, as follows:

$$l_G = V_G \Delta t$$

$$x_{k+n} = x_{k+n-1} + \Delta l \, cos\varphi_{k+n-1}; \quad n = 1 \ldots \frac{l_G}{\Delta l}$$

$$y_{k+n} = y_{k+n-1} + \Delta l \, sin\varphi_{k+n-1}; \quad n = 1 \ldots \frac{l_G}{\Delta l}$$

$$\varphi_k^n = \varphi_{k-1}^n + \sqrt{\frac{2\Delta l}{l_p}} \Theta$$

Where, k is the index of the last point in the previous time step and l_p is the persistence length of the branches (set to 150 μm, Supplementary Table 2). Additionally, the Δl value of the last point is adjusted if l_G is not an integer multiple of Δl. Θ is a unit Gaussian variable centered at zero.

While shrinking, points from the branches are removed until the shrinking length $l_S = V_S \Delta t$ is reached.

Contact-based retraction:

It has been shown by several studies that Dscam molecules play an important role in the self-avoidance of dendritic tips in Class IV neurons (Matthews et al., 2007; Soba et al., 2007). To investigate the phenomenon, we measured the dynamics of the dendritic tips after a collision/contact event has occurred. Interestingly, we observed that the transition rates are altered after contact as shown in Table 1B and leads to an overall shrinkage of the dendritic tips. To implement this observation in the model, we assumed that the contact is achieved whenever a tip comes very close (<0.15 μm, ~average radius of branches, Supplementary Table 2) to a nearby branch. Further, we used the altered tip dynamical parameters after a tip makes a contact (post-contact). Because it is difficult to measure how long the tips remain in their post-contact dynamics, we added this as a free parameter in the model (Supplementary Table 2). It was chosen to be longer than the expected lifetimes of post-contact dendrites (10-15 minutes).

Boundary Condition:

Individual Class IV neurons grow within the hemi-segments (Grueber et al., 2002). We have experimentally measured the segment sizes in the AP and LR directions at different developmental stages as shown in the inset to Figure 1. Linearly fits to the growing region (24 to 96 hr) defined the growth rates of the boundary used in our model. Because there is self-avoidance interaction between the neighboring neurons, we used a periodic boundary condition.

Initial condition:

To avoid any ambiguity in the initial timepoint in the simulation, we divided the simulation process into two halves. We started our simulation at 14 hr with 2-4 randomly oriented branches of length ~15 μm and allowed them to grow with the 18 hr tip dynamics data (Table 1 A) and the 24 hr branching rate. When the dendritic tree reached the measured value of total branch number at 24 hr, we reassigned this time as 24 hr. In this way, we simulated larval morphogenesis.

Initial Lag

There is an unexpected paucity of dendrite deaths at short times. To analyze this, we calculated the survival probability of the branches in the following way:

Suppose dendritic tips are born and die throughout the observation period T. Divide T into small equal intervals dt. Let,

$f(0)$ = Number{die in time $[0, dt)$}/Number{alive at time 0}

$f(dt)$ = Number{die in time $[dt, 2dt)$}/Number{alive at time dt}

$f(2dt)$ = Number{die in time $[2dt, 3dt)$}/Number{alive at time $2dt$} …etc.

Then we can write the survival probability as:

$$D(t) = \prod_{i=0}^{t/dt} [1 - f(i)]$$

The survival probability of the experimentally observed dendritic tips was measured manually and then calculated by using the above formula. This is shown by the solid black line in Supplementary Figure 4 A. The survival curve does not decay exponentially which led us to conclude that the tips have some initial period of sustained growth which we termed as initial lag τ_{lag}. To estimate the amount of initial lag we simulated 1000 free tips with 48 hr tip dynamics data (because it is in the middle of the developmental time) and implemented an initial lag (τ_{lag}) during which the tips did not switch into the

paused or shrinking states ($K_{GP} = K_{GS} = 0; t \leq \tau_{lag}$). We calculated the survival probability by dividing number of alive branches by the total number of branches. The survival probability increases with the initial lag τ_{lag} as shown by the dotted lines in Supplementary Figure 4A. The dark blue is the best fit to the real data (τ_{lag} = 0.3 min, Supplementary Table 2) and we used this value in our model.

Markovian tests of the tip trajectories

The tip dynamics is not a 'Markovian process'. The non-Markovian traits are shown by the presence of initial lag during nascent branch formation (τ_{lag}) and the change of dynamics after contact (Supplementary Table 2). However, the dynamics is a first-order process as shown by the single exponential decay of phase durations as shown in Supplementary Figure 3 D-F which points towards the fact that the dynamics don't have any long-term memory. To confirm this, we calculated the state-state auto-correlation function (data not shown). The average autocorrelation function quickly becomes uncorrelated showing the absence of any long-term memory in the states.

Key model parameters

The agent-based model contains 67 parameters: 4 for the velocity distribution and 6 for the transition rates (times 4 for 24, 48 and 96 hr and post-collision, Table 1 and Supplementary Tables 1 -2), 3 for the exponential fit to branching rates (24, 36, 48, 72 and 96 hr, Supplementary Table 1), 8 from Supplementary Table 2, 2 for the initial condition and 4 for the boundary condition. It is instructive to ask which parameters are key for determining dendrite morphology. We therefore performed a sensitivity analysis. The boundary was omitted to monitor the unconstrained arbor growth rate.

Branching increases arbor growth and density (Supplementary Figure 5 B). When the branching frequency was increased 2-fold, with all other parameters equal, the cell width increased ~20%, leading to a ~50% increase in cell area. The number of branches increased 3-fold, the total branch length increased 2-fold and the average branch length decreased 30%, with a small increase in the fractal dimension. Decreasing branching frequency had the opposite effects.

The stochasticity of tip growth (its variability) increases arbor growth without changing density (Supplementary Figure 5 B). When all the transition rates were decreased 2-fold, which does not change in the average tip velocity but makes tips grow more stochastically, the arbor width grew 40% faster, leading to a doubling of arbor area. The branch number and total branch length also doubled, so the mean branch length remained unchanged, as did the fractal dimension. Increasing the transition rates, which decreases the stochasticity, had the opposite effect.

Increasing the average tip velocity increases arbor growth with little effect on density (Supplementary Figure 5 C). When the average tip velocity was increased 2-fold by increasing the tip growth velocity, the arbor width grew 50% faster, with a 2.2-fold increase in area. There was a corresponding increase in branch points and total branch length, and so no effect on mean branch length, though there was a small increase in fractal dimension. Decreasing the average tip velocity 2-fold had the opposite effect. When the tip velocity was set to zero (Supplementary Figure 5 C), the arbor still grew, but only at half the rate of the control: despite the 4-fold decrease in area, there was

little effect on density, mean branch length, though the fractal dimension decreased. When the tip velocity was made negative (-0.02 μm/min), the arbor failed to grow and was more open, with an increase in mean branch length and a decrease in fractal dimension.

The branching angle is also a key parameter (data not shown). Decreasing the branching angle to 45° (i.e., more distal) increased the growth rate. Increasing the branching angle to 135° has the opposite effect. We previously noted that several parameters have little effect, including the persistence length, the post-contact time. Furthermore, the interaction length, soma radius, and initial length are not expected to have dramatic effects.

In summary, branching, a positive average tip velocity, and tip stochasticity all drive arbor growth. Arbors can even grow when the average tip velocity is zero. Branching increases the density of the arbor, whereas tip velocity (and its variability) has little effect on density. The branching angle strongly affects arbor growth and the prolonged growth after birth also contributes to the burst of branch formation at early times (Figure 6D).

Supplementary Figures

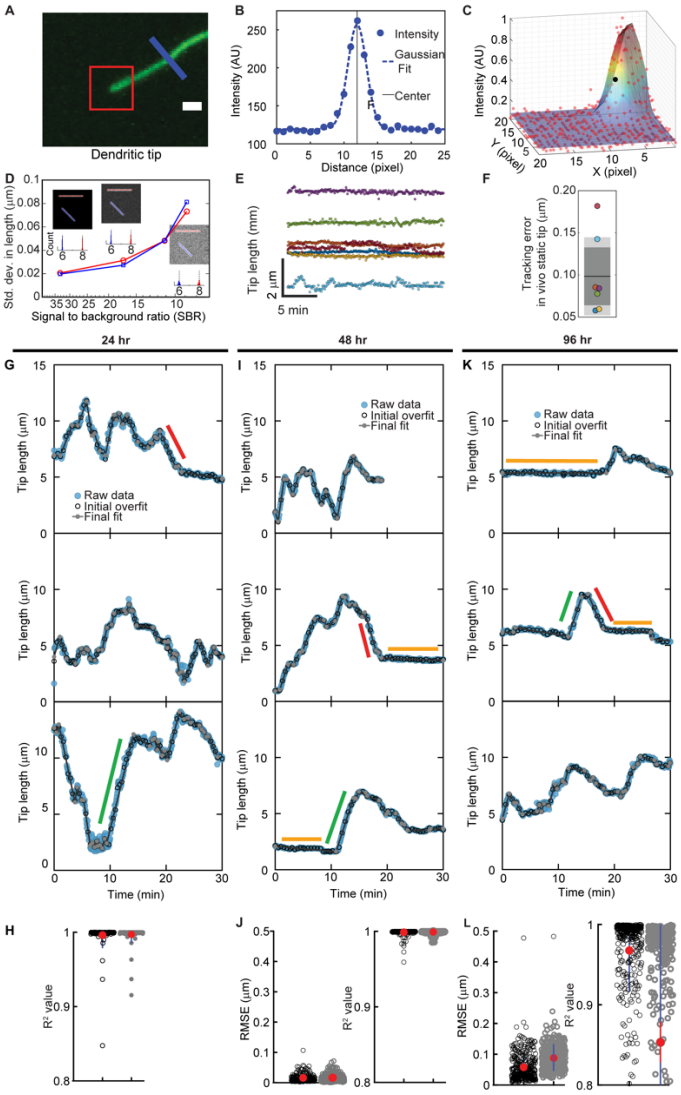

Supplementary Figure 1. Tracking dendrite tips. **A** Example of a fluorescently labeled terminal dendrite. **B** The center of the dendrite was located by fitting the cross-sections (blue line in B) to a Gaussian. The precision is approximately 0.1 µm. **C** The position of the tip of the dendrite was calculated by fitting the end intensity profile (red box in A) to a 2D function corresponding to a Gaussian in the perpendicular direction and an error function the parallel direction (see Methods) **D** Montage of simulated images of cylindrical tubes (6 µm blue, 8 µm red) that are fluorescently labeled with 10% labeling density on the surface with signal-to-background ratio (SBR), defined as the mean signal divided by the standard deviation of background noise, varying from 33 (left) to 9 (right). The pixel size is 100 nm. The measured length distribution is shown in the bottom panel (200 independently generated images for each SBR). **E** The standard deviation of the measured length is plotted against the SBR. The accuracy is high even for the lowest SBRs. **F** The lengths of several live-imaged dendrites that were in their paused state as a function of time. **G** The standard deviation of the tracked lengths is ~1 pixel (108 nm). Examples of tracked dendritic length as a function of time: **G** 24 hr. **I** 48 hr. and **K** 96 hr. The green, orange, and red lines denote examples of growing, paused, and shrinking states. The tips tend to spend more time in the paused state over developmental time. **H**, **J**, and **L** show the statistics of the piecewise-linear fitting.

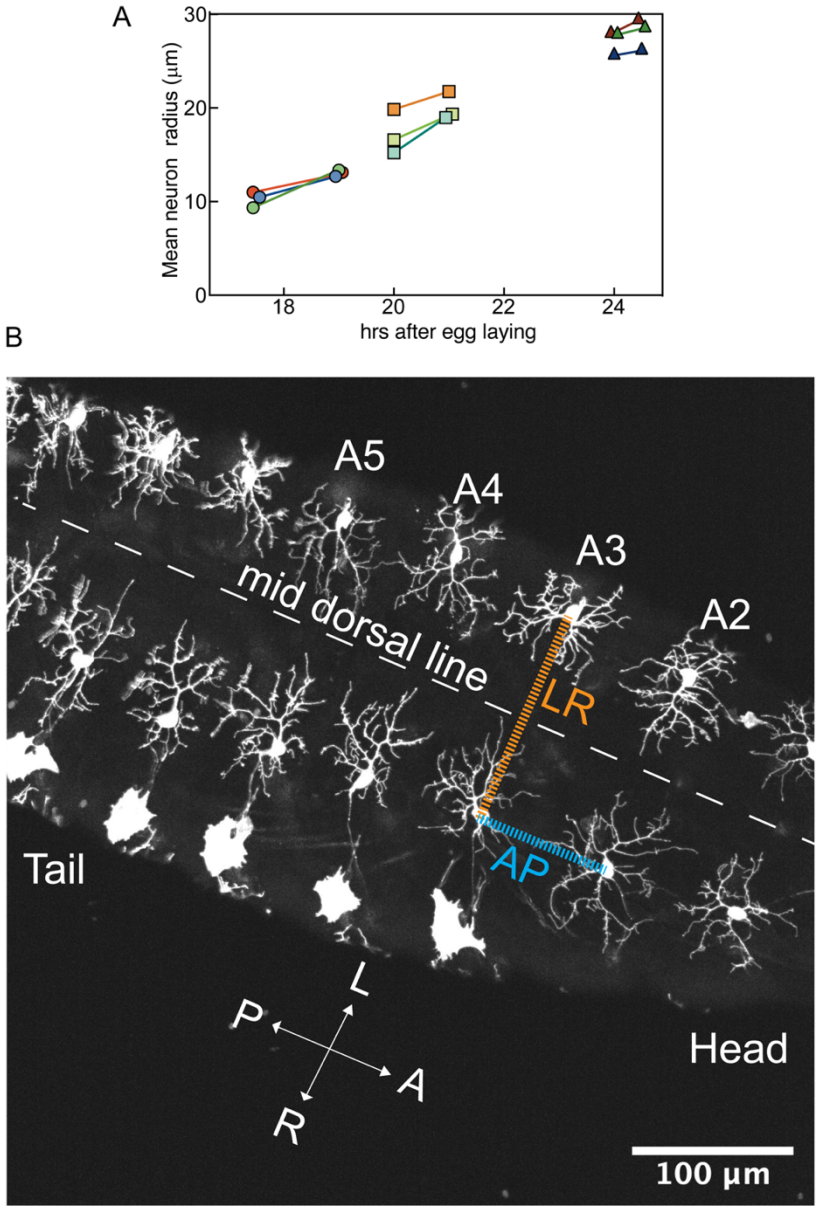

Supplementary Figure 2. A Control showing that imaging does not perturb growth. The growth of cells is assessed by measuring the rate of increase of their overall radius (calculated as √(area/π)) while imaging. Lines connect cells at the beginning and end of imaging. This shows that the imaging conditions do not retard growth.**B** Definitions of the anterior-posterior (**AP**) and left-right (**LR**) axes. A2, A3, A4, and A5 corresponds to the dorsal abdominal segments. The white dashed line is the dorsal midline and defines the AP axis. This larva is ~24 hr after egg lay.

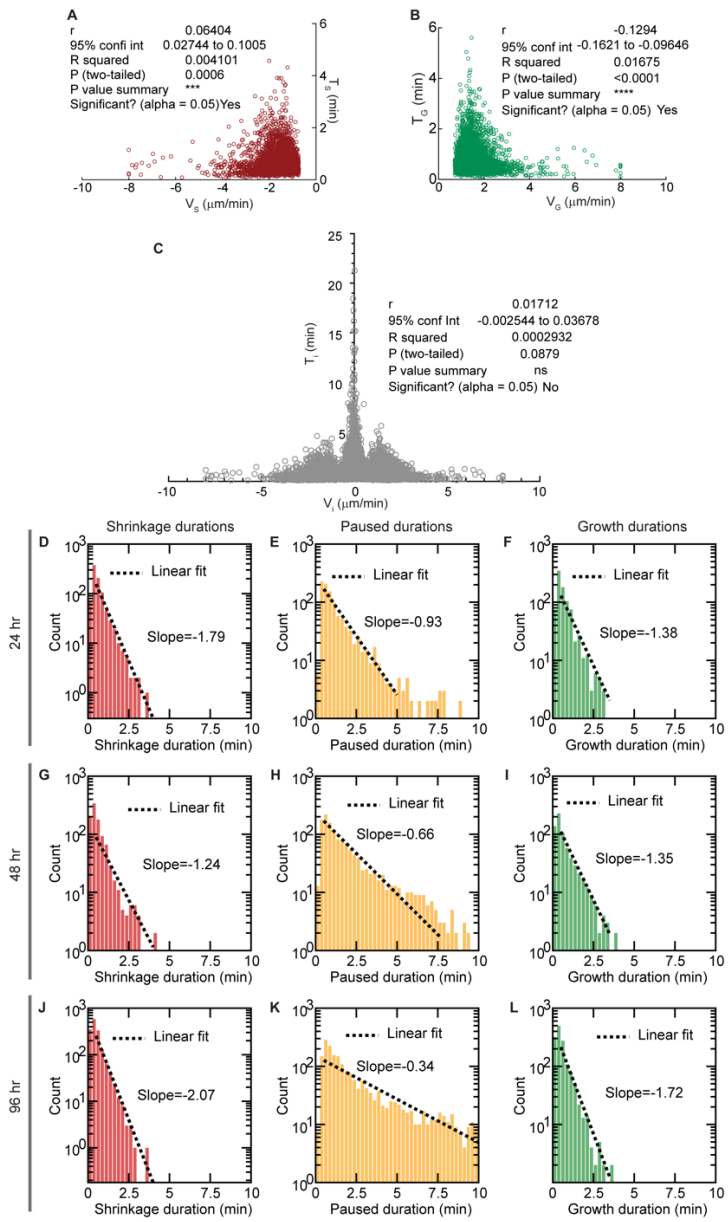

Supplementary Figure 3: Correlation between state velocities and lifetimes and state durations: A The correlation between shrinking velocities (V_S) and shrinking lifetimes (T_S) shows a significant correlation with Pearson's correlation coefficient r=0.064. **B** Similarly, a significant correlation is observed between growth velocities (V_G) and growth lifetimes (T_G)**. C** Pearson's correlation coefficient (r) between state velocities (V_i) and lifetimes (T_i) for 18-20 hr data. The value of r is small (0.017) and there is no significant correlation between V_i and T_i. The distribution durations for the shrinking (S), paused (P), and growing (G) states at 24 hr (**A-F**), 48 hr (**G-I**), and 96 hr (**J-L**) plotted using semi-log axes. The distributions are very close to exponentials (dotted lines) expected if switching among the states is first order. The slope of the dotted lines is the inverse of the lifetimes spent in the states: for example, at 24 hr, the sum of the transition rates from growing state is ($K_{GP} + K_{GS} = 0.696 + 0.509 = 1.205$ min^{-1} (Table 1 A), close to the slope of the lifetime distribution of 1.38 min^{-1} (F).

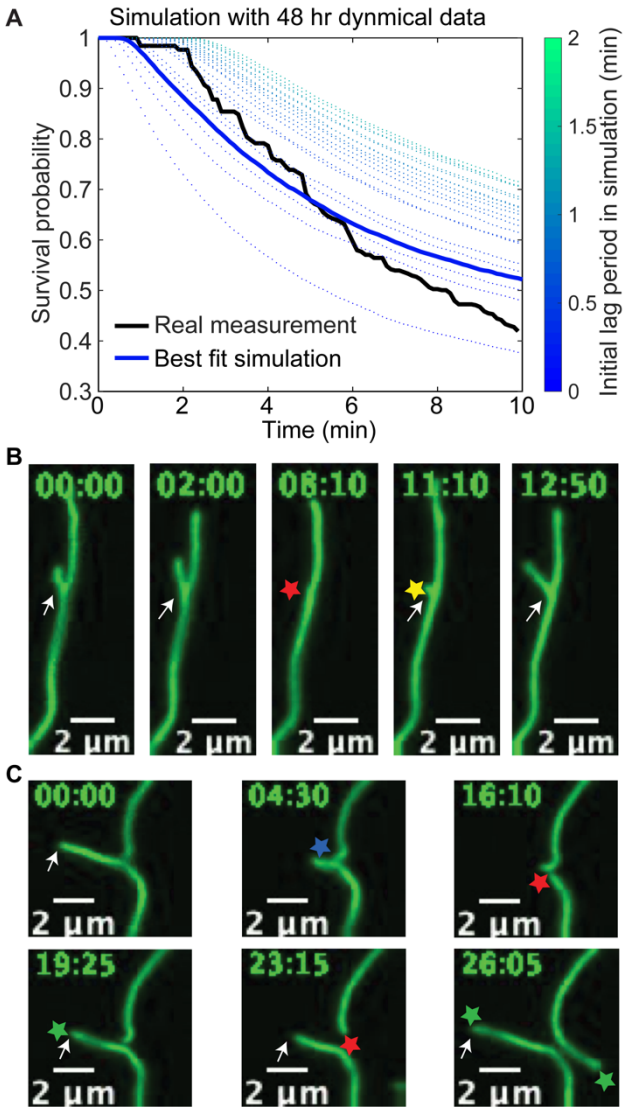

Supplementary Figure 4: Evidence for persistent growth after birth. A We manually measured the time between branch initiation and branch death at different stages of the larva (24, 48,72, and 96 hr AEL, 3 movies for each stage). From these data, we calculated the survival probability by dividing the number of alive branches by the total number of branches using the formula described in the Methods. The black line is the average survival probability of the real dendrite tips. The survival probability does not start decaying exponentially as one might expect if it were a Poisson process. Rather, it shows some initial lag. This observation led us to believe that branch initiation is not a simple Poisson process. To estimate the initial lag period, we simulated 1000 branches with initial length 0.5 μm and implemented a lag time (τ_{lag}) by preventing the tips to switch into the paused or shrinkage state ($K_{GP} = K_{GS} = 0; t \leq \tau_{lag}$). A branch is deleted in the simulation when its length is <0.1 μm. The survival probability increases with the initial lag τ as shown by the dotted lines. The dark blue is the best fit to the real data (τ_{lag} = 0.3 min). **B** An example of branch retraction and regrowth from the same point. White arrows correspond to the region where a branch exists and then disappear and branched again. **C** An example of a branch that collided with another branch, retracted, and then followed the previous path during regrowth (white arrows). Red star corresponds to shrinkage, yellow star corresponds to the birth of a branch, blue star corresponds to collision event, and green star shows tip growth.

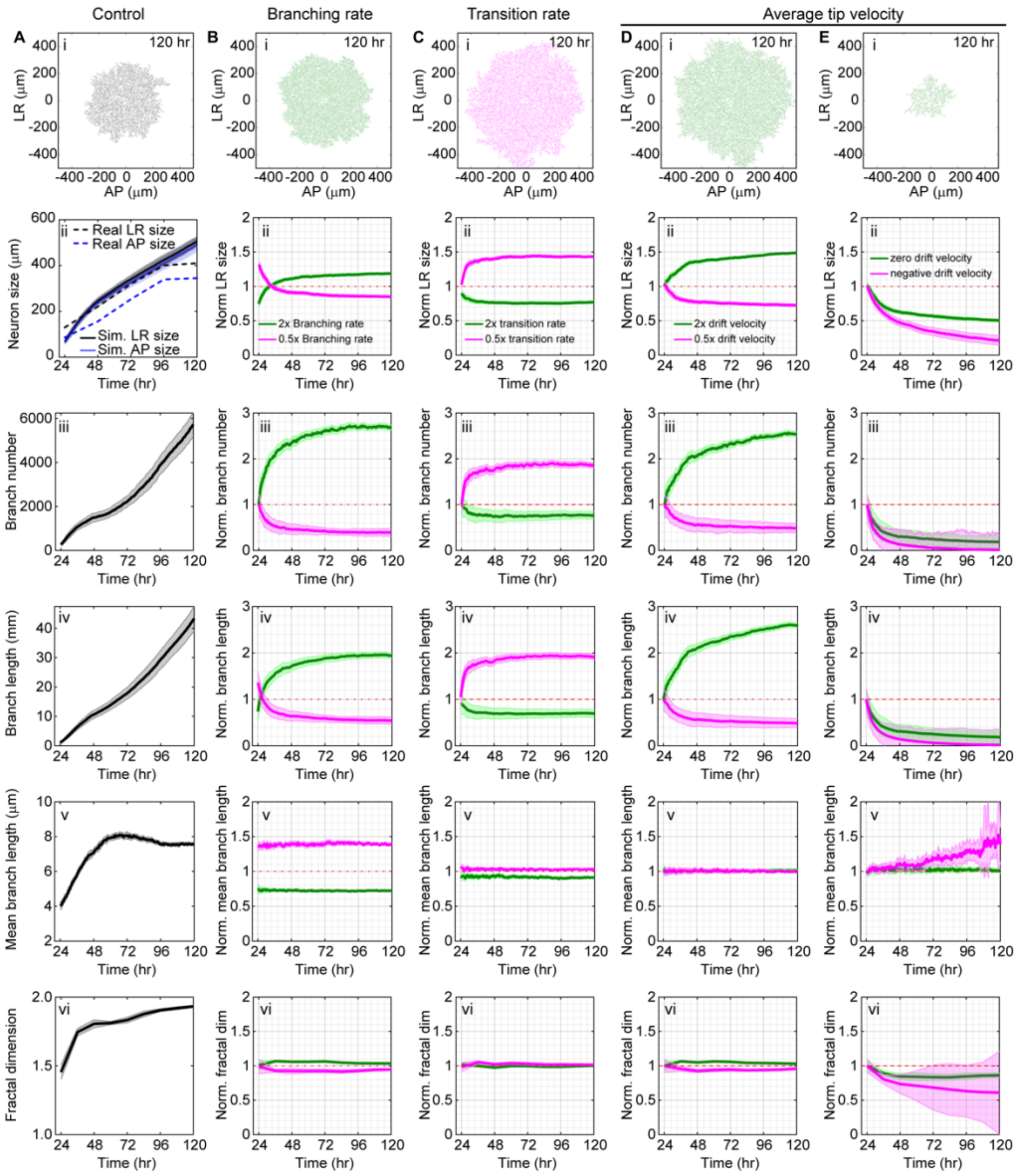

Supplementary Figure 5: **Sensitivity of morphology to branching and growth parameters**: **A** Control with parameters from Table 1 and Supplementary Tables 1-2 without any boundary restriction. The black and blue lines represent LR and AP sizes respectively. The solid lines represent the simulated segment sizes over development. The simulation shows that initially (24-48 hr) the neurons grow faster than the real segment and then grow with a constant rate equal to the segment growth rate (~0.06 μm/min) until 96 hr. The segment widths saturate after 96 hr even without a boundary. **B** Branching rate was doubled (green) and halved (magenta) compared to the control, keeping all other parameters unchanged. All arbor properties are normalized by the respective unconstrained controls. Fold change is plotted against time for (ii) arbor size, (iii) branch number, (iv) branch length, (v) mean branch length, and (vi) fractal dimension. **C** All transition rates were doubled (green) and halved (magenta): this leads to a decrease and increase in the variability of growth. **D** The mean tip velocity (drift) was increased (green) and decreases (magenta) 2-fold. **E** The average (drift) velocity was set to zero (green) and a negative value (-0.02 /min, magenta). Shaded regions represent standard error of mean.

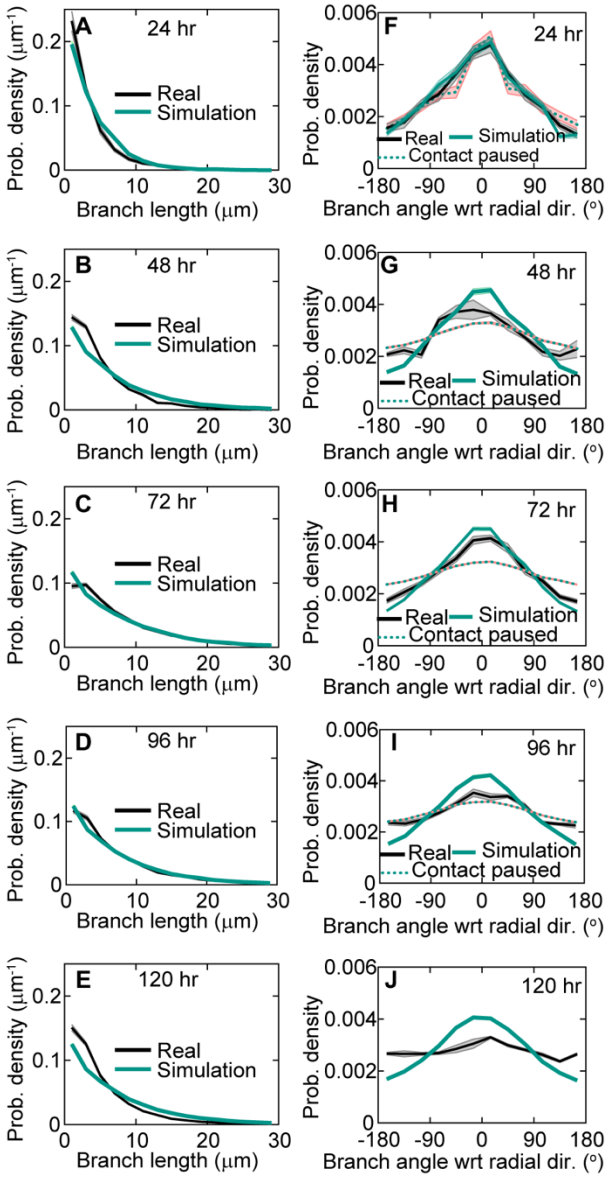

Supplementary Figure 6: **Branch length and radial orientation distributions**: **A-E** Branch length distribution over different developmental stages for real and simulated arbors. **F-J** Radial orientation of branches over developmental time for real and simulated arbors. The branches are preferentially oriented in the radial direction. This preference is due to contact-based retraction. The dotted curves show diminished radial preference when branches are paused after contact in the simulation.

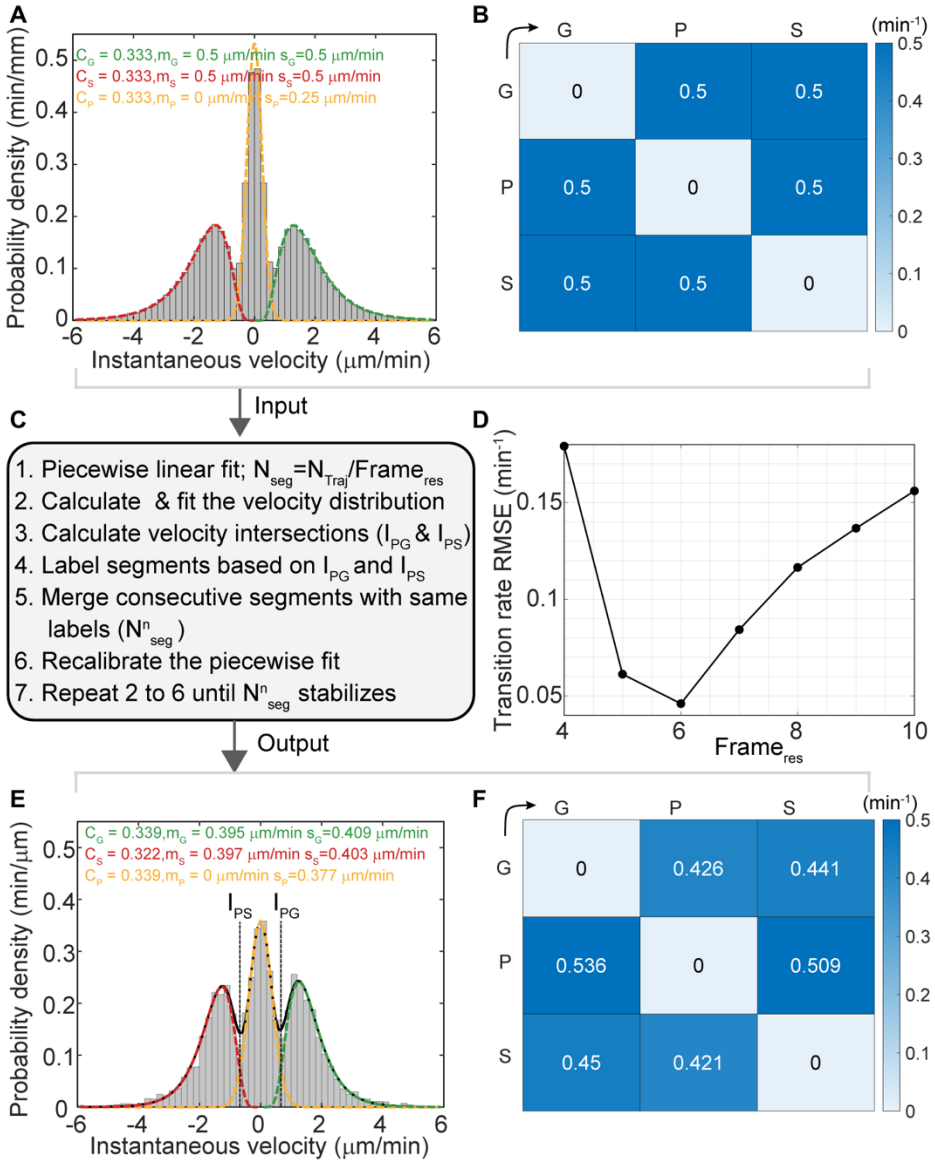

Supplementary Figure 7: Validation of trajectory analysis method. We simulated 200 Markov trajectories with realistic input parameters shown in **A** and **B** and then added Gaussian white noise on the individual points of the trajectories. We used the transition rate as 0.5 /min because of the observed fact that the individual states last ~1 minute. **C** The flowchart of the trajectory analysis method. **D** We varied the Frame resolution to find the optimal resolution. The root-mean-squared error between the input and output transition rate matrix is plotted as a function of frame resolution. Frame resolution of 6 provides the best result and we chose this value for all our analyses. **E** &**F** The output velocity distribution and transition rate matrix using frame resolution 6. Our method of analysis produced a faithful reproduction of the input parameters.

Supplementary Tables

Supplementary Table 1: Branching rates

Age (hr)	Total branching rate[a] (min^{-1}) (Mean ± SD)	Linear branching rate[b] ($\mu m^{-1} \cdot min^{-1}$) (Mean ± SD)	Branching angle[c] (°) (Mean ± SD)	Numbers (rates, angles)
18 (E)	4.26 ± 0.59	0.0109 ± 0.0015	85 ± 25	$n = 9,5$
24 (L1)	7.59 ± 1.52	0.0095 ± 0.0017	88 ± 26	$n = 9,7$
36 (L1)	5.77 ± 2.67	0.0031 ± 0.0009	85 ± 25	n = 6,7
48 (L2)	4.86 ± 1.59	0.0019 ± 0.0007	86 ± 26	n = 6,4
72 (L2)	8.31 ± 2.37	0.0011 ± 0.0004	90 ± 25	n = 6,5
96 (L3)	11.12 ± 2.52	0.0011 ± 0.0006	91 ± 25	n = 6,4

[a]Over the entire dendrite arbor
[b]Per total dendrite length
[c]Angle between dendrites is zero in the distal direction of the mother.
Standard deviation (SD).

Supplementary Table 2: Model parameters

Name	Description	Value
l_{initial}	Initial length of nascent branch	0.50 μm
$l_{\text{interaction}}$	Length scale of contact	0.15 μm
$\tau_{\text{post-contact}}$	Post-contact dynamics duration	15 min
τ_{lag}	Initial lag of nascent branch	0.3 min
l_{P}	Persistence length	150 μm
R_{soma}	Radius of soma	10 μm
μ_b^θ	Mean branching angle	$\pi/2$
σ_b^θ	Standard dev. of branching angle	$\pi/7$

Supplementary Table 3: Mutations

Mutation	Reference	Morphology	Features of mutants	Simulated neuron	Parameters
Non-uniform branching					
Dynein intermediate light chain (Dlic)	(Arthur et al., 2015; Satoh et al., 2008; Zheng et al., 2008)	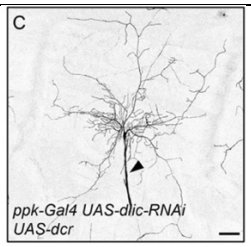 Fig 2C (Arthur et al., 2015)	Defective axonal and dendritic morphology, downsizing of the overall arbor, shift of branching activity to the proximal area within the arbor. Neurons fail to tile.		Non uniform branching, primary branch has basal branching rate.
Lis-1	(Liu et al., 2000; Satoh et al., 2008; Zheng et al., 2008)	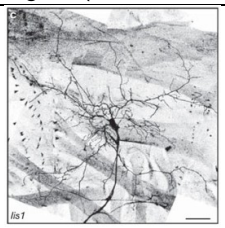 Fig 1C (Zheng et al., 2008)	Reduced dendritic arborization in flies (similar to dlic) and mice. Neurons fails to tile.		
Change in tip dynamics					
katanin	(Stewart et al., 2012)	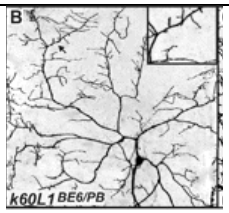 Fig 3B (Stewart et al., 2012)	Decreased dendritic branch number, length, and arbor coverage in class IV neurons	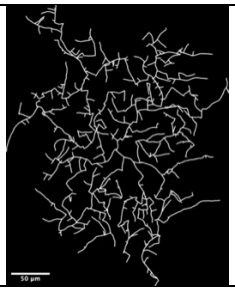	Terminal branches spend less time in the paused state and more time in the retracting phase.
Self-avoidance					
Trc	(Emoto et al., 2004)	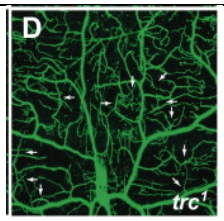 Fig 1D (Emoto et al., 2004)	Excessive terminal branching and fail to avoid homologous dendritic branches, resulting in significant overlap of the dendritic fields.	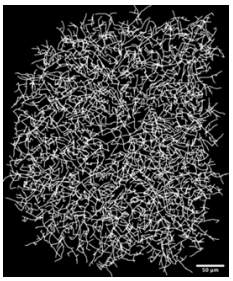	Branches are allowed to cross 10 % of the time.
Dscam	(Hughes et al., 2007; Matthews et al., 2007; Soba et al., 2007)	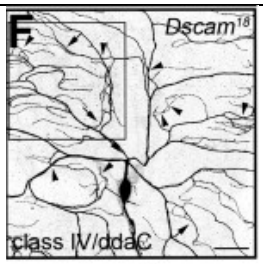 Fig 1F (Soba et al., 2007)	Branch curling, crossing over, reduced self-avoidance, dendrite bundling. No effect on tiling.		

Supplementary movies

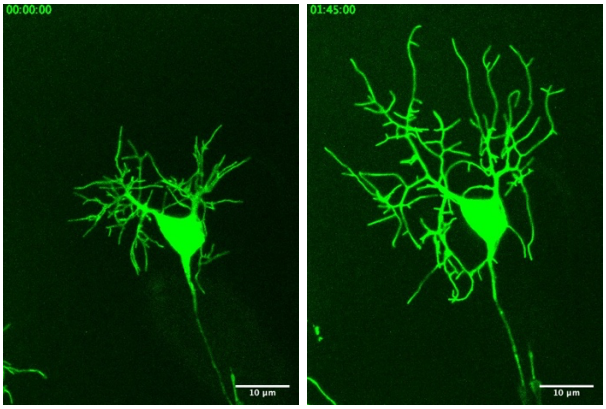

Supplementary movie 1. Time-lapse movie of a growing neuron: Time lapse movie of an embryonic neuron at 17.5hr AEL was acquired using a spinning disk confocal microscope. The movie was full-frame (2048x 2048 pixels) and a complete stack of images (7um) was produced every 5 mins interval.

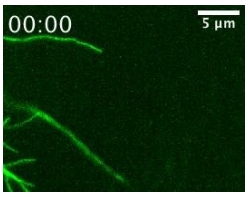

Supplementary movie 2. Tip growth and branching

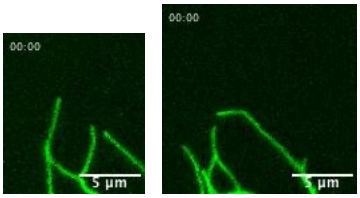

Supplementary movie 3. Self-avoidance and shrinkage

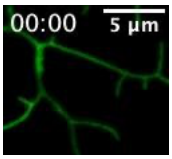

Supplementary movie 4. Self-avoidance and growth

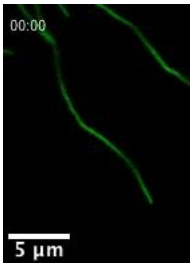

Supplementary movie 5. Tip pause

Supplementary movie 6-10. Tip growth, bending, and branching. Dendrite lengthening is likely due to the addition of materials at the dendrite tip. The green stars show dendrite tip lengthening, the yellow star is birth of new branch, and the red star is a shrinkage event. White arrows point to the bending of growing tips. In example two, where the branch disappears, a sharp bend smoothens over time. In examples 3,4, and 5, the white arrows correspond to structural features such as branches and bends that remain fixed during growth and shortening.

Dendrite lengthening example 1

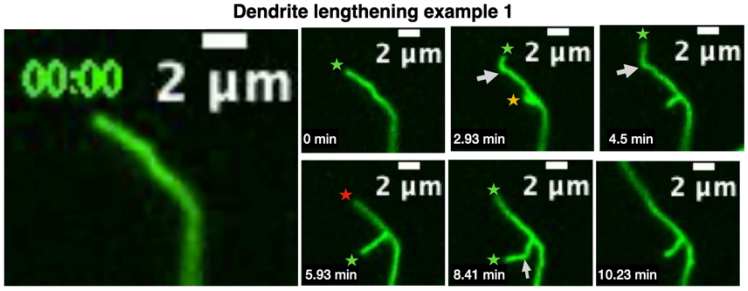

Dendrite lengthening example 2

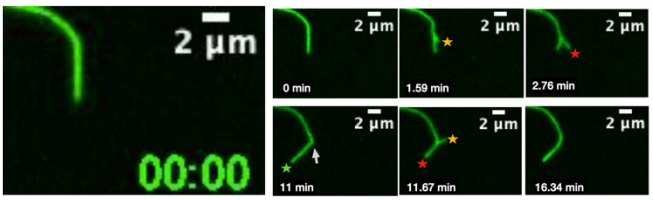

Dendrite lengthening example 3

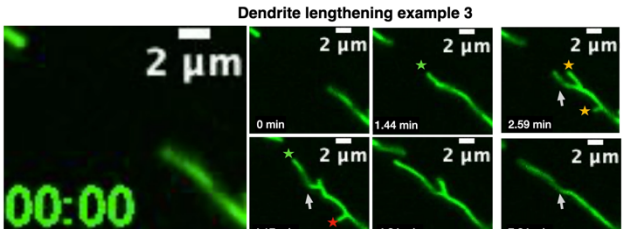

Dendrite lengthening example 4

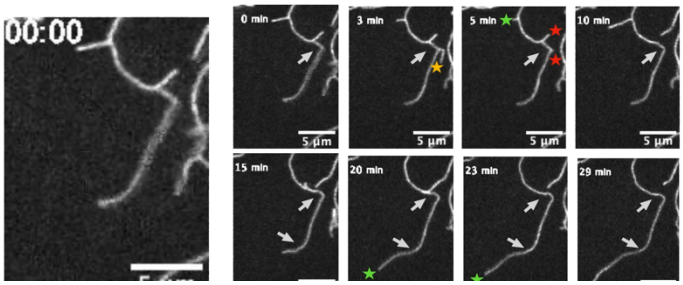

Dendrite lengthening example 5

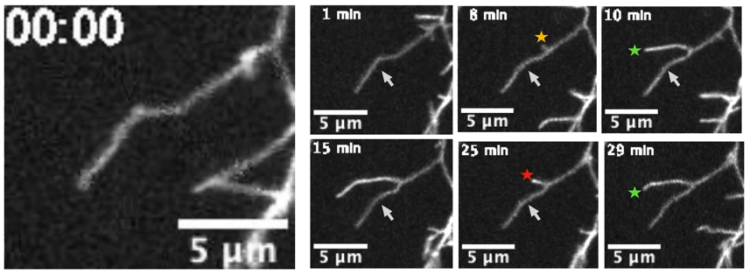

1178 **References**
1179

1180 Arthur, A.L., Yang, S.Z., Abellaneda, A.M., and Wildonger, J. (2015). Dendrite
1181 arborization requires the dynein cofactor NudE. J Cell Sci *128*, 2191–2201.

1182 Ascoli, G.A., and Krichmar, J.L. (2000). L-neuron: A modeling tool for the efficient
1183 generation and parsimonious description of dendritic morphology. Neurocomputing *32*–
1184 *33*, 1003–1011.

1185 Baltruschat, L., Tavosanis, G., and Cuntz, H. (2020). A developmental stretch-and-fill
1186 process that optimises dendritic wiring. Biorxiv 2020.07.07.191064.

1187 Basak, R., Sutradhar, S., and Howard, J. (2021). Focal Laser Stimulation of Fly
1188 Nociceptors Activates Distinct Axonal and Dendritic Ca2+ Signals. Biophys J.

1189 Cajal, S.R. (1995). Histology of the nervous system of man and vertebrates. History of
1190 Neuroscience (Oxford Univ Press, New York).

1191 Cajal, S.R. y (1906). The Structure and Connexions of Neurons. Nobel Lecture.

1192 Castro, A.F., Baltruschat, L., Stürner, T., Bahrami, A., Jedlicka, P., Tavosanis, G., and
1193 Cuntz, H. (2020). Achieving functional neuronal dendrite structure through sequential
1194 stochastic growth and retraction. Elife *9*, e60920.

1195 Cuntz, H., Forstner, F., Borst, A., and Häusser, M. (2010). One Rule to Grow Them All:
1196 A General Theory of Neuronal Branching and Its Practical Application. Plos Comput Biol
1197 *6*, e1000877.

1198 Decker, F., Oriola, D., Dalton, B., and Brugués, J. (2018). Autocatalytic microtubule
1199 nucleation determines the size and mass of Xenopus laevis egg extract spindles. ELife
1200 *7*, 6656.

1201 DeFelipe, J., López-Cruz, P.L., Benavides-Piccione, R., Bielza, C., Larrañaga, P.,
1202 Anderson, S., Burkhalter, A., Cauli, B., Fairén, A., Feldmeyer, D., et al. (2013). New
1203 insights into the classification and nomenclature of cortical GABAergic interneurons.
1204 Nature Reviews Neuroscience *14*, 202–216.

1205 Delandre, C., Amikura, R., and Moore, A.W. (2016). Microtubule nucleation and
1206 organization in dendrites. Cell Cycle *15*, 1–8.

1207 Demchouk, A.O., Gardner, M.K., and Odde, D.J. (2011). Microtubule Tip Tracking and
1208 Tip Structures at the Nanometer Scale Using Digital Fluorescence Microscopy. Cell Mol
1209 Bioeng *4*, 192–204.

Denk, W., Briggman, K.L., and Helmstaedter, M. (2012). Structural neurobiology: missing link to a mechanistic understanding of neural computation. Nat Rev Neurosci *13*, 351–358.

Dent, E.W., Gupton, S.L., and Gertler, F.B. (2011). The growth cone cytoskeleton in axon outgrowth and guidance. Csh Perspect Biol *3*, a001800–a001800.

D'Errico, J. (2021). SLM-Shape Language Modeling (Mathworks).

Dogterom, M., and Leibler, S. (1993). Physical aspects of the growth and regulation of microtubule structures. Physical Review Letters *70*, 1347–1350.

Dong, X., Shen, K., and Bülow, H.E. (2015). Intrinsic and Extrinsic Mechanisms of Dendritic Morphogenesis. Annu Rev Physiol *77*, 1–30.

Emoto, K., He, Y., Ye, B., Grueber, W.B., Adler, P.N., Jan, L.Y., and Jan, Y.-N. (2004). Control of Dendritic Branching and Tiling by the Tricornered-Kinase/Furry Signaling Pathway in Drosophila Sensory Neurons. Cell *119*, 245–256.

Falconer, K. (1990). Fractal Geometry: Mathematical Foundations and Applications (Chichester ; New York : Wiley).

Fornito, A., Zalesky, A., and Breakspear, M. (2015). The connectomics of brain disorders. Nat Rev Neurosci *16*, 159–172.

Forrest, M.P., Parnell, E., and Penzes, P. (2018). Dendritic structural plasticity and neuropsychiatric disease. Nat Rev Neurosci *19*, 215–234.

Ganguly, S., Trottier, O., Liang, X., Bowne-Anderson, H., and Howard, J. (2016). Morphology of Fly Larval Class IV Dendrites Accords with a Random Branching and Contact Based Branch Deletion Model.

Gao, F.-B., Brenman, J.E., Jan, L.Y., and Jan, Y.N. (1999). Genes regulating dendritic outgrowth, branching, and routing in Drosophila. Gene Dev *13*, 2549–2561.

Grueber, W.B., Jan, L.Y., and Jan, Y.N. (2002). Tiling of the Drosophila epidermis by multidendritic sensory neurons. Dev Camb Engl *129*, 2867–2878.

Grueber, W.B., Ye, B., Moore, A.W., Jan, L.Y., and Jan, Y.N. (2003). Dendrites of distinct classes of Drosophila sensory neurons show different capacities for homotypic repulsion. Current Biology *13*, 618–626.

Han, C., Wang, D., Soba, P., Zhu, S., Lin, X., Jan, L.Y., and Jan, Y.N. (2012). Integrins regulate repulsion-mediated dendritic patterning of drosophila sensory neurons by restricting dendrites in a 2D space. Neuron *73*, 64–78.

1242 Hannezo, E., Scheele, C.L.G.J., Moad, M., Drogo, N., Heer, R., Sampogna, R.V.,
1243 Rheenen, J. van, and Simons, B.D. (2017). A Unifying Theory of Branching
1244 Morphogenesis. Cell *171*, 242-255.e27.

1245 Hansen, P.C., and O'Leary, D.P. (1993). The Use of the L-Curve in the Regularization
1246 of Discrete Ill-Posed Problems. Siam J Sci Comput *14*, 1487–1503.

1247 Hughes, M.E., Bortnick, R., Tsubouchi, A., Bäumer, P., Kondo, M., Uemura, T., and
1248 Schmucker, D. (2007). Homophilic Dscam Interactions Control Complex Dendrite
1249 Morphogenesis. Neuron *54*, 417–427.

1250 Jan, Y.-N., and Jan, L.Y. (2010). Branching out: mechanisms of dendritic arborization.
1251 Nat Rev Neurosci *11*, 316–328.

1252 Jinushi-Nakao, S., Arvind, R., Amikura, R., Kinameri, E., Liu, A.W., and Moore, A.W.
1253 (2007). Knot/Collier and Cut Control Different Aspects of Dendrite Cytoskeleton and
1254 Synergize to Define Final Arbor Shape. Neuron *56*, 963–978.

1255 Kanari, L., Dłotko, P., Scolamiero, M., Levi, R., Shillcock, J., Hess, K., and Markram, H.
1256 (2018). A Topological Representation of Branching Neuronal Morphologies.
1257 Neuroinformatics *16*, 3–13.

1258 Kandel, E.R., Markram, H., Matthews, P.M., Yuste, R., and Koch, C. (2013).
1259 Neuroscience thinks big (and collaboratively). Nat Rev Neurosci *14*, 659–664.

1260 Kapitein, L.C., and Hoogenraad, C.C. (2015). Building the Neuronal Microtubule
1261 Cytoskeleton. Neuron *87*, 492–506.

1262 Kelliher, M.T., Yue, Y., Ng, A., Kamiyama, D., Huang, B., Verhey, K.J., and Wildonger,
1263 J. (2018). Autoinhibition of kinesin-1 is essential to the dendrite-specific localization of
1264 Golgi outposts. J Cell Biol *217*, 2531–2547.

1265 Kim, M.E., Shrestha, B.R., Blazeski, R., Mason, C.A., and Grueber, W.B. (2012).
1266 Integrins Establish Dendrite-Substrate Relationships that Promote Dendritic Self-
1267 Avoidance and Patterning in Drosophila Sensory Neurons. Neuron *73*, 79–91.

1268 Kirschner, M., and Mitchison, T. (1986). Beyond self-assembly: from microtubules to
1269 morphogenesis. *45*, 329–342.

1270 Koleske, A.J. (2013). Molecular mechanisms of dendrite stability. Nat Rev Neurosci *14*,
1271 536–550.

1272 Komarova, Y.A., Vorobjev, I.A., and Borisy, G.G. (2002). Life cycle of MTs: persistent
1273 growth in the cell interior, asymmetric transition frequencies and effects of the cell
1274 boundary. Journal of Cell Science *115*, 3527–3539.

1275 Kulkarni, V.A., and Firestein, B.L. (2012). The dendritic tree and brain disorders. Mol
1276 Cell Neurosci *50*, 10–20.

1277 Lee, A., Li, W., Xu, K., Bogert, B.A., Su, K., and Gao, F.-B. (2003). Control of dendritic
1278 development by the Drosophila fragile X-related gene involves the small GTPase Rac1.
1279 Development *130*, 5543–5552.

1280 Lefebvre, J.L., Sanes, J.R., and Kay, J.N. (2013). Development of Dendritic Form and
1281 Function. Annu Rev Cell Dev Bi *31*, 1–37.

1282 Lefevre, J.G., Short, K.M., Lamberton, T.O., Michos, O., Graf, D., Smyth, I.M., and
1283 Hamilton, N.A. (2017). Branching morphogenesis in the developing kidney is governed
1284 by rules that pattern the ureteric tree. Development (Cambridge, England) *144*, 4377–
1285 4385.

1286 Li, W., and Gao, F.-B. (2003). Actin Filament-Stabilizing Protein Tropomyosin Regulates
1287 the Size of Dendritic Fields. J Neurosci *23*, 6171–6175.

1288 Liang, X., Kokes, M., Fetter, R.D., Sallee, M.D., Moore, A.W., Feldman, J.L., and Shen,
1289 K. (2020). Growth cone-localized microtubule organizing center establishes microtubule
1290 orientation in dendrites. Elife *9*, e56547.

1291 Liao, M., Liang, X., and Howard, J. (2021). The narrowing of dendrite branches across
1292 nodes follows a well-defined scaling law. Proc National Acad Sci *118*, e2022395118.

1293 Liu, Z., Steward, R., and Luo, L. (2000). Drosophila Lis1 is required for neuroblast
1294 proliferation, dendritic elaboration and axonal transport. Nat Cell Biol *2*, 776–783.

1295 Longair, M.H., Baker, D.A., and Armstrong, J.D. (2011). Simple Neurite Tracer: open
1296 source software for reconstruction, visualization and analysis of neuronal processes.
1297 Bioinformatics *27*, 2453–2454.

1298 Lowery, L.A., and Vactor, D.V. (2009). The trip of the tip: understanding the growth cone
1299 machinery. Nat Rev Mol Cell Bio *10*, 332–343.

1300 Lu, P., and Werb, Z. (2008). Patterning mechanisms of branched organs. Sci New York
1301 N Y *322*, 1506–1509.

1302 Luczak, A. (2006). Spatial embedding of neuronal trees modeled by diffusive growth. J
1303 Neurosci Meth *157*, 132–141.

1304 Matthews, B.J., Kim, M.E., Flanagan, J.J., Hattori, D., Clemens, J.C., Zipursky, S.L.,
1305 and Grueber, W.B. (2007). Dendrite Self-Avoidance Is Controlled by Dscam. Cell *129*,
1306 593–604.

1307 Metzger, R.J., Klein, O.D., Martin, G.R., and Krasnow, M.A. (2008). The branching
1308 programme of mouse lung development. Nature *453*, 745–750.

1309 Mitchison, T., and Kirschner, M. (1984). Dynamic instability of microtubule growth.
1310 Nature *312*, 237–242.

1311 Moughamian, A.J., and Holzbaur, E.L.F. (2017). Dyneins. In Cytoplasmic Dynein
1312 Dysfunction and Neurodegenerative Disease, S.M. King, ed. (Academic Press), pp.
1313 286–315.

1314 Nanda, S., Das, R., Bhattacharjee, S., Cox, D.N., and Ascoli, G.A. (2018).
1315 Morphological determinants of dendritic arborization neurons in Drosophila larva. Brain
1316 Struct Funct *223*, 1107–1120.

1317 Nithianandam, V., and Chien, C.-T. (2018). Actin blobs prefigure dendrite branching
1318 sites. J Cell Biol *217*, 3731–3746.

1319 Ori-McKenney, K.M., Jan, L.Y., and Jan, Y.-N. (2012). Golgi Outposts Shape Dendrite
1320 Morphology by Functioning as Sites of Acentrosomal Microtubule Nucleation in
1321 Neurons. Neuron *76*, 921–930.

1322 Palavalli, A., Tizón-Escamilla, N., Rupprecht, J.-F., and Lecuit, T. (2021). Deterministic
1323 and Stochastic Rules of Branching Govern Dendrite Morphogenesis of Sensory
1324 Neurons. Curr Biol *31*, 459-472.e4.

1325 Parrish, J.Z., Xu, P., Kim, C.C., Jan, L.Y., and Jan, Y.N. (2009). The microRNA bantam
1326 Functions in Epithelial Cells to Regulate Scaling Growth of Dendrite Arbors in
1327 Drosophila Sensory Neurons. Neuron *63*, 788–802.

1328 Petry, S., Groen, A.C., Ishihara, K., Mitchison, T.J., and Vale, R.D. (2013). Branching
1329 microtubule nucleation in Xenopus egg extracts mediated by augmin and TPX2. *152*,
1330 768–777.

1331 Pollard, T.D., and Borisy, G.G. (2003). Cellular Motility Driven by Assembly and
1332 Disassembly of Actin Filaments. Cell *112*, 453–465.

1333 Robertson, J.L., Tsubouchi, A., and Tracey, W.D. (2013). Larval Defense against Attack
1334 from Parasitoid Wasps Requires Nociceptive Neurons. Plos One *8*, e78704.

1335 Ruhnow, F., Zwicker, D., and Diez, S. (2011). Tracking single particles and elongated
1336 filaments with nanometer precision. Biophys J *100*, 2820–2828.

1337 Sánchez-Soriano, N., Tear, G., Whitington, P., and Prokop, A. (2007). Drosophila as a
1338 genetic and cellular model for studies on axonal growth. Neural Dev *2*, 9–9.

1339 Satoh, D., Sato, D., Tsuyama, T., Saito, M., Ohkura, H., Rolls, M.M., Ishikawa, F., and
1340 Uemura, T. (2008). Spatial control of branching within dendritic arbors by dynein-
1341 dependent transport of Rab5-endosomes. Nat Cell Biol *10*, 1164–1171.

1342 Scott, E.K., Reuter, J.E., and Luo, L. (2003). Small GTPase Cdc42 is required for
1343 multiple aspects of dendritic morphogenesis. J Neurosci Official J Soc Neurosci *23*,
1344 3118–3123.

1345 Sears, J.C., and Broihier, H.T. (2016). FoxO regulates microtubule dynamics and
1346 polarity to promote dendrite branching in Drosophila sensory neurons. Dev Biol *418*,
1347 40–54.

1348 Seung, S. (2012). Connectome: How the Brain's Wiring Makes Us Who We Are.

1349 Sherwood, N.T., Sun, Q., Xue, M., Zhang, B., and Zinn, K. (2004). Drosophila Spastin
1350 Regulates Synaptic Microtubule Networks and Is Required for Normal Motor Function.
1351 Plos Biol *2*, e429.

1352 Short, K.M., Combes, A.N., Lefevre, J., Ju, A.L., Georgas, K.M., Lamberton, T.,
1353 Cairncross, O., Rumballe, B.A., McMahon, A.P., Hamilton, N.A., et al. (2014). Global
1354 Quantification of Tissue Dynamics in the Developing Mouse Kidney. Dev Cell *29*, 188–
1355 202.

1356 Singhania, A., and Grueber, W.B. (2014). Development of the embryonic and larval
1357 peripheral nervous system of Drosophila. Wiley Interdiscip Rev Dev Biology *3*, 193–210.

1358 Smith, M.B., Li, H., Shen, T., Huang, X., Yusuf, E., and Vavylonis, D. (2010).
1359 Segmentation and tracking of cytoskeletal filaments using open active contours.
1360 Cytoskelet Hoboken N J *67*, 693–705.

1361 Soba, P., Zhu, S., Emoto, K., Younger, S., Yang, S.-J., Yu, H.-H., Lee, T., Jan, L.Y., and
1362 Jan, Y.-N. (2007). Drosophila Sensory Neurons Require Dscam for Dendritic Self-
1363 Avoidance and Proper Dendritic Field Organization. Neuron *54*, 403–416.

1364 Stewart, A., Tsubouchi, A., Rolls, M.M., Tracey, W.D., and Sherwood, N.T. (2012).
1365 Katanin p60-like1 Promotes Microtubule Growth and Terminal Dendrite Stability in the
1366 Larval Class IV Sensory Neurons of Drosophila. J Neurosci *32*, 11631–11642.

1367 Stoeckli, E.T. (2018). Understanding axon guidance: are we nearly there yet?
1368 Development *145*, dev151415.

1369 Stürner, T., Tatarnikova, A., Mueller, J., Schaffran, B., Cuntz, H., Zhang, Y.,
1370 Nemethova, M., Bogdan, S., Small, V., and Tavosanis, G. (2019). Transient localization
1371 of the Arp2/3 complex initiates neuronal dendrite branching in vivo. Development *146*,
1372 dev.171397.

1373 Sugimura, K., Shimono, K., Uemura, T., and Mochizuki, A. (2007). Self-organizing
1374 Mechanism for Development of Space-filling Neuronal Dendrites. Plos Comput Biol *3*,
1375 e212.

1376 Tessier-Lavigne, M., and Goodman, C.S. (1996). The Molecular Biology of Axon
1377 Guidance. Science *274*, 1123–1133.

1378 Toner, J., and Tu, Y. (1995). Long-Range Order in a Two-Dimensional Dynamical XY
1379 Model: How Birds Fly Together. Physical Review Letters *75*, 4326–4329.

1380 Vicsek, T., Czirók, A., Ben-Jacob, E., Cohen, I., and Shochet, O. (1995). Novel Type of
1381 Phase Transition in a System of Self-Driven Particles. Phys Rev Lett *75*, 1226–1229.

1382 Weiner, A.T., Lanz, M.C., Goetschius, D.J., Hancock, W.O., and Rolls, M.M. (2016).
1383 Kinesin-2 and Apc function at dendrite branch points to resolve microtubule collisions.
1384 Cytoskeleton (Hoboken, NJ) *73*, 35–44.

1385 Winding, M., Kelliher, M.T., Lu, W., Wildonger, J., and Gelfand, V.I. (2016). Role of
1386 kinesin-1-based microtubule sliding in Drosophila nervous system development. P Natl
1387 Acad Sci Usa *113*, E4985-94.

1388 Yalgin, C., Ebrahimi, S., Delandre, C., Yoong, L.F., Akimoto, S., Tran, H., Amikura, R.,
1389 Spokony, R., Torben-Nielsen, B., White, K.P., et al. (2015). Centrosomin represses
1390 dendrite branching by orienting microtubule nucleation. Nat Neurosci *18*, 1437–1445.

1391 Yang, W.-K., and Chien, C.-T. (2019). Beyond being innervated: the epidermis actively
1392 shapes sensory dendritic patterning. Open Biol *9*, 180257.

1393 Zheng, Y., Wildonger, J., Ye, B., Zhang, Y., Kita, A., Younger, S.H., Zimmerman, S.,
1394 Jan, L.Y., and Jan, Y.N. (2008). Dynein is required for polarized dendritic transport and
1395 uniform microtubule orientation in axons. Nat Cell Biol *10*, 1172–1180.

1396 Zheng, Z., Lauritzen, J.S., Perlman, E., Robinson, C.G., Nichols, M., Milkie, D., Torrens,
1397 O., Price, J., Fisher, C.B., Sharifi, N., et al. (2018). A Complete Electron Microscopy
1398 Volume of the Brain of Adult Drosophila melanogaster. Cell *174*, 730-743.e22.

1399